

POLITECNICO DI TORINO

MASTER's Degree in  
PHYSICS OF COMPLEX SYSTEMS



MASTER's Degree Thesis

MODELS OF CELL MEMBRANE PATTERNING  
VIA DIFFUSION-CONTROLLED  
PHASE SEPARATION

Supervisor

Prof. ANDREA GAMBA

Candidate

GABRIELE RIGANO

DECEMBER 2022

# Summary

It has been recently recognized that phase separation phenomena play a central role in the formation of the spatially-localized intracellular compartments that allow eukaryotic cells to perform their vital functions. Experiments show that the selforganization of biomolecules in localized cytosolic compartments exhibits several features of classical quasi-equilibrium *liquid-liquid* phase separation, such as the existence of an interfacial tension and of a critical size for the nucleation of germs of a new phase. On the other hand, biological processes are known to take place far from equilibrium and to involve active, energy-consuming enzymatic processes. In this thesis I analyze a realistic, multicomponent, out-of-equilibrium model for the selforganization of a two-dimensional *gas* of signaling molecules into spatially localized domains on cell membranes, driven by enzymatic self-reinforcing feedback loops. Numerical simulations of the model show the emergence of the whole phenomenology of classical phase separation, including the organization into distinct phases, nucleation of germs of a more stable phase in the “sea” of a homogeneous metastable phase, competitive domain growth (“coarsening”), domain coalescence, and relaxation at large times to a statistical steady state characterized by a single domain of the new phase. This emerging phenomenology is analyzed by comparing the numerical results with the predictions of a coarse-grained Landau-Ginzburg description of the system in terms of a single-component order parameter. Overall, these results suggest that a “classical” phase separation phenomenology on cell membranes can result from the out-of equilibrium dynamics of a complex system of enzymatic reactions, leading to the formation of “soft” (gas-like) localized domains enriched in specific chemical factors. In addition, I report preliminary results on the selforganization of domains enriched in distinct signaling proteins (Rab5 and Rab11) on endosomal membranes from experiments that I performed during my internship at IRCCS Candiolo.

# Table of contents

<b>1</b>	<b>Introduction</b>	<b>3</b>
<b>2</b>	<b>Phenomenology of classical phase separation</b>	<b>5</b>
<b>3</b>	<b>Active vs passive phase separation</b>	<b>7</b>
<b>4</b>	<b>Phase separation in cell biology</b>	<b>9</b>
<b>5</b>	<b>Diffusion-controlled phase separation</b>	<b>11</b>
5.1	Model description	11
5.2	Mass action kinetics	14
5.3	Landau-Ginzburg dynamics	15
5.3.1	Time evolution of a circular domain	16
5.3.2	Structure of the phase boundary	19
5.3.3	Interfacial tension	20
<b>6</b>	<b>Numerical results</b>	<b>23</b>
6.1	Simulation protocol	23
6.1.1	Microscopic units	25
6.2	Phenomenology of diffusion-controlled phase separation	25
6.2.1	Nucleation, coarsening, and relaxation to the steady state	25
	Homogeneous nucleation	26
	Heterogeneous nucleation	33
6.2.2	Domain coalescence	40
6.3	Single domain growth	43
6.3.1	Comparison between numerical and theoretical domain growth dynamics	45
6.3.2	Measure of interfacial tension	46
6.3.3	Parameter dependence of interfacial tension	46
6.4	Multiple domain growth	47
<b>7</b>	<b>Experimental investigation of Rab5-Rab11 co-localization in endosomes</b>	<b>49</b>
7.1	Immunofluorescence technique	49
7.2	Colocalization study	50
7.3	Interpretation of the experimental results	51
7.4	Limitations of the study	51
<b>8</b>	<b>Discussion</b>	<b>53</b>
	<b>Appendix A Experimental Materials and Methods</b>	<b>55</b>
	<b>Bibliography</b>	<b>57</b>



# Chapter 1

## Introduction

*Phase separation* is the process by which a homogeneous mixture of different molecules spontaneously separates in two coexisting phases characterized by different concentrations of one or more molecular species. In the last decades phase separation has been observed to have a crucial role in many biological function taking place in membraneless compartments, biomolecular condensates concentrating proteins and nucleic acids [10, 4].

In order to perform such functions, compartments biogenesis, maintenance and disassembly must be finely controlled, and the mechanisms of phase separation are responsible for such fine control. For example in, *germ-cell specification* is mediated by localization to the posterior of cell embryo of P-granules (Fig. 4.2), membraneless compartments composed of proteins and RNAs. Such localization is driven by phase separation.

Phase separation is also used by the cells to promote *signaling outputs* on membranes.

In particular, in Ref. [14], a 12-component signaling pathway have been reconstituted on *model membranes* (supported lipid bilayers). The input of the pathway is T-cell receptor (TCR) phosphorylation, while the output is actin assembly. Upon TCR phosphorylation, the signaling proteins have been observed to organize in clusters on the membrane recruiting and organizing actin regulators (Fig. 4.1) [14]. Without phase separation mechanism, spatial control on actin assembly couldn't occur. Phase separation occurs also on endosome membranes, here specific proteins, Rab5, Rab11, Rab7 are observed to organize in distinct domains on the membrane of the same endosome, and their quantities depend on the fate of the transported cargo, therefore on *endosome maturation stage* [13, 11].

It's clear that pattern formation, induced by phase separation, is crucial for cellular functions to occur properly, since all the involved macromolecules (lipids, enzymes, nucleic acids, signaling molecules...), are well localized and compartmentalized in time and space. In the present work, we focus on phase separation taking place on cell membranes, based on biochemical interactions between the constituents, and on their ability to diffuse.

The problem will be studied combining a coarse-grained (phase-field) description, than can be partially treated analytically, and a numerical model simulating the reaction-diffusion equations in a three-dimensional environment. A comparison between our model, and the classical one, will be performed: the same phenomenology will be observed, and analogies between fundamental parameters of the two model will be revealed.



## Chapter 2

# Phenomenology of classical phase separation

In this section the main mechanisms and features of classical phase separation will be exposed.

Having a homogeneous mixture of molecules, separated phases emerge when the action of demixing, driven by electrostatic interaction is stronger than the thermal agitation tendency to mix the components of a mixture. The beginning of this process is characterized by the nucleation of a germ of the more stable phase, such nucleation occurs due to stochastic fluctuations (homogeneous nucleation) or due to presence of nucleation centers induced by some external perturbation (heterogeneous nucleation). This initial stage is called **nucleation**.

A single germ can eventually grow, depending on the balance between exportation and importation of molecules from the solution. Of course, more than one nucleation germ can arise and start growing, however they will compete for the growth. During this stage (**coarsening**), the larger domains grow at the expense of the smaller ones, due to their evaporation, until only one remains and an equilibrium is reached between the two phases (**relaxation to the steady state**). Eventually, during the coarsening stage, more than one domain can fuse together, creating a larger and more stable one (**coalescence**).

Some observable features characterizing the phase separation are expressed below:

- I. During the process, the interface area (or perimeter length in two-dimensional systems) between the two phases tends to be minimized, leading to the formation of approximately spherical (or *circular*, in two-dimensional systems) growing *domains*.
- II. If coarsening occurs close to thermodynamic equilibrium, the coarsening process itself can be seen as a competition between a bulk energy, given by the increasing volume (or surface in 2D) of the domain, and a surface free energy, proportional to the increasing interface surface area (or perimeter in 2D). The proportionality constant is the *interfacial tension* ( $\sigma$ ).
- III. If the initial seeds are not sufficiently large, (below the *critical size*), they are going to disappear favoring the growth of sufficiently large domains.
- IV. The speed of coarsening is determined by the *degree of metastability*  $\psi$ . In the first instants  $\psi$  is high, and the process is fast. As time proceeds  $\psi$  decreases, the number of domains decreases, and the growth of the remaining ones slows down.
- V. The critical size ( $R_c$ ), is inversely proportional to  $\psi$ , therefore it increases up to the equilibrium size of the domain ( $R_{eq}$ ).

To fix idea, let's consider a binary mixture of species A and B. The species are characterized by homotypic intermolecular affinity, meaning that a molecule of a certain type can interact only with molecule of the same type. Such system can be fully described, studying the difference between the two phase concentration, we will call this quantity *order parameter*  $\phi$ . Since the molecules diffuse without being created or destroyed  $\phi$  is said to be *locally conserved*, and its dynamics is described by the Cahn-Hilliard equation (Eq. 2.3) [3]

$$f = \frac{K}{2} |\nabla \phi|^2 + V(\phi) \quad (2.1)$$

$$\mathcal{F}[\phi] = \int \left[ \frac{K}{2} |\nabla \phi|^2 + V(\phi) \right] d\mathbf{r} \quad (2.2)$$

$$\frac{\partial \phi(\mathbf{r}, t)}{\partial t} = \nabla^2 \left[ \frac{\delta \mathcal{F}[\phi]}{\delta \phi(\mathbf{r}, t)} \right] \quad (2.3)$$

In (2.2) the gradient term increases the value of free energy due to the presence of the interface between the two phases, while the potential  $V(\phi)$  denotes the strength of interactions. In such description  $V(\phi)$  can develop two minimas, each one corresponding to the two possible phases, which can coexist in two different regions of the space (Fig. 2.1).

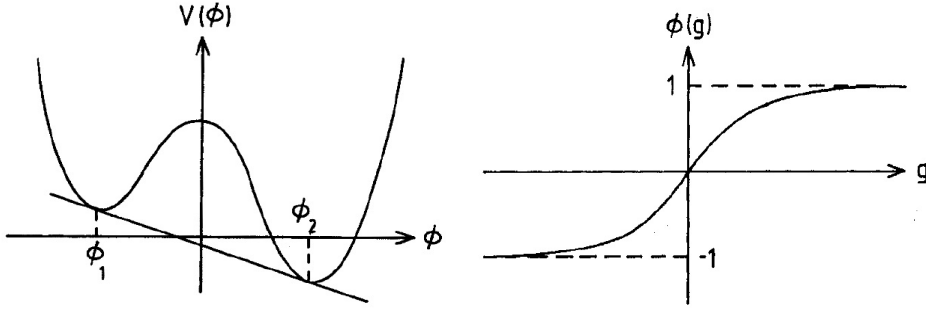


**Figure 2.1.** (Left) Asymmetric potential  $V(\phi)$  in case of a conserved order parameter  $\phi$ . (Right) Order parameter as a function of a coordinate ( $g$ ) normal to the interface [3]

## Chapter 3

# Active vs passive phase separation

Most of the biological functions are intrinsically non-equilibrium. Macromolecules participating to this functions are often involved in transport and enzymatic processes, during which they continuously and irreversibly consume energy. These are *active* features of the living matter, and cannot be explained in the context of classical phase separation, since, relying on concepts of *equilibrium statistical mechanics*, it cannot describe non equilibrium processes.

In literature, different versions of classical phase separation, have been proposed to describe phase separation phenomena in biological environment. Some of them simply reproduce the passive features of the classical model [2, 14], others, reproduce some of the mentioned active features.

For example, in emulsions of droplets in a fluid, Ostwald ripening, a coarsening process, is suppressed in the case in which the droplets can autocatalyze their own droplet material [17]. Here, by introducing an *active* feature (enzymatic reactions inside the droplets) to a classical model of phase separation, coarsening is suppressed.

In chapter 5, we are going to introduce a model for phase separation which takes into account transport phenomena and enzymatic reactions (active features).



## Chapter 4

# Phase separation in cell biology

The paradigm of biological phase separation proposes that compartments, i.e different regions characterized by different phases, are liquid-like, and are formed by demixing of a unique homogeneous phase. The intermolecular reactions driving this process are weak, adhesive and unspecific, and are based on the electrical properties of the macromolecules, rather than specific functions or interactions that characterize such macromolecules [1, 10].

We have already anticipated that phase separation plays a central role in some biological processes, such as: signaling outputs promotion on membranes [14], germ cell specification in *C. elegans* [2], cargo transportation through endosomes [13, 11]. In all this processes at least one stage of classical phase separation phenomenology is observed.

Nucleation of pLAT (linker for activation of T cells) and binding signaling proteins is shown in Fig. 4.1. Coalescence of P-granules droplets is shown in Fig. 4.2, and distinct domains of Rab5 and Rab11 are observed on endosome membranes (Fig. 4.3).

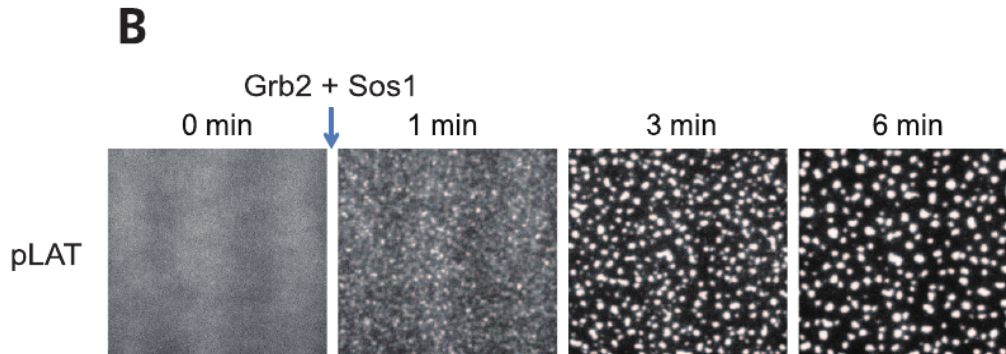


**Figure 4.1.** Nucleation of pLAT (linker for activation of T cells) and binding signaling proteins upon TCR phosphorylation (Grb2+Sos1 insertion) [14].

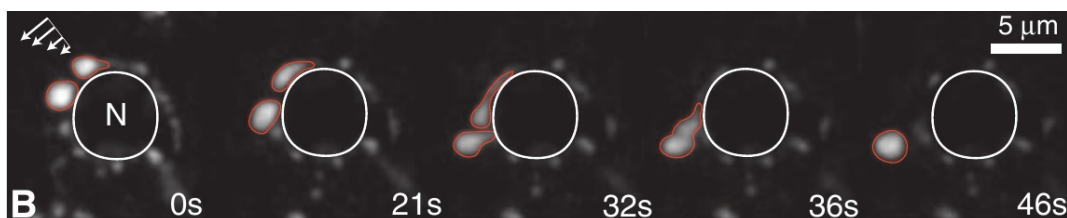


**Figure 4.2.** Coalescence of P-granules droplets. Fusion of P-granules droplets (red outlines) suggests their liquid behavior. A coalescence event is occurring between 32s and 36s. Nucleus (N), white line [2].

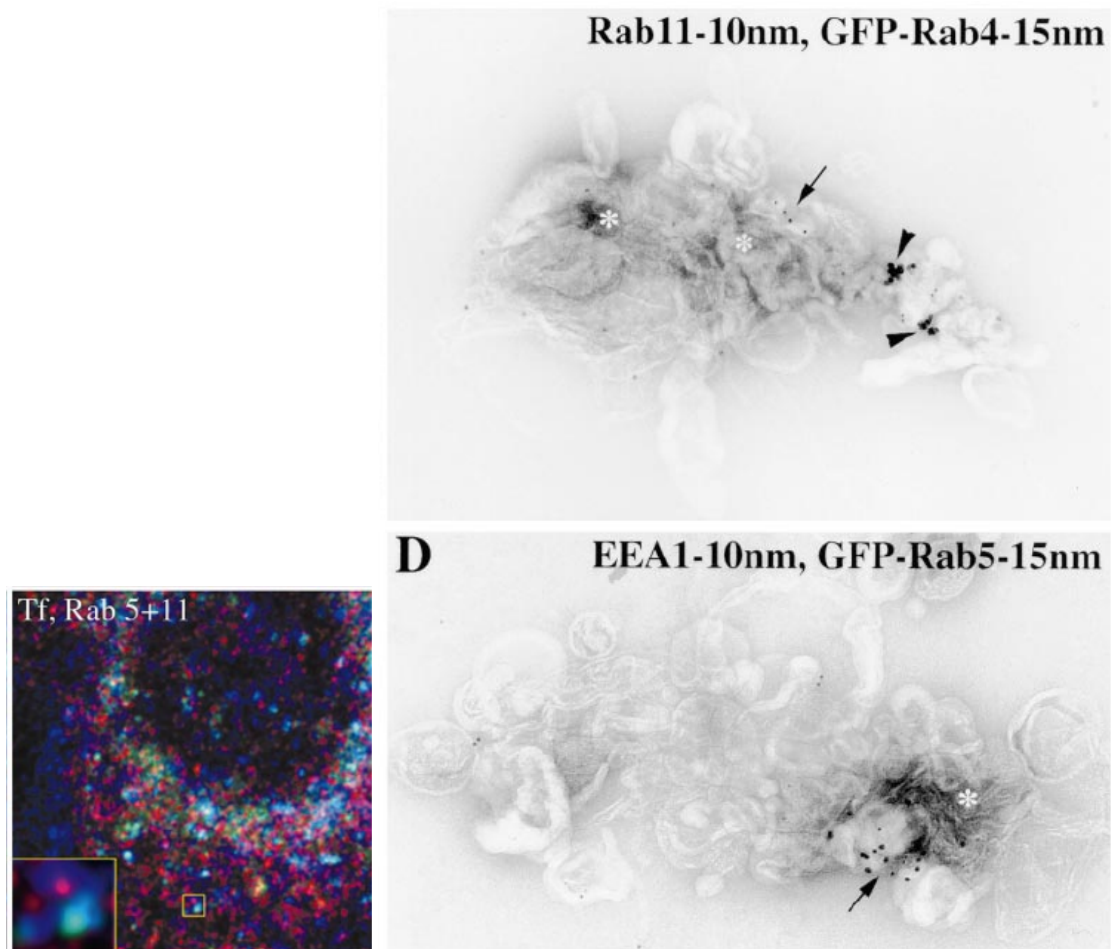


**Figure 4.3.** Rab5 and Rab11 domains on the same endosome membrane. Confocal fluorescence microscopy shows co-localization of Rab5 (blue), Rab11 (red) and Transferrin (green) on the same endosome membrane (Left). Electron microscopy of Rab5 and Rab11 coupled to gold particles shows distinct domains of the proteins on membranes.

# Chapter 5

## Diffusion-controlled phase separation

Classical phase separation is not the only paradigm that explain the phenomenology of phase separation. It has been observed that reaction-diffusion systems [7, 5, 6, 15, 12], which are based on *biochemical interactions* between the constituents, and on their ability to *diffuse*, are able to provide a good description of the phase separation phenomenology on membranes. Moreover, since, transport phenomena and enzymatic reactions are taken into account, they reproduce some of the active features of biological processes [4].

In the present discussion this paradigm will be called *diffusion-controlled phase separation*. In this model, the weak interactions characterizing the classical model are substituted by effective interactions mediated by enzymatic feedback loops, therefore the intermolecular distance between the constituents is larger than their typical size. This is a feature that can be attributed to gas rather than liquids, therefore it is interesting that a gas-like system can behave as a liquid.

Diffusion-controlled phase separation is studied combining three different approaches: mass action kinetics, Landau-Ginzburg and stochastic approach.

### 5.1 Model description

In this section we will qualitatively describe the *biochemical network* constituting our model.

We investigate a reaction-diffusion system describing the mutual conversion of two generic membrane-bounded species (A, B). Such species can be identified with lipids, proteins, RNAs, distinct signaling molecules, or different states of the same molecules [9, 6].

The mutual conversion is mediated by the action of free cytosolic enzymes ( $E_B, E_A$ ) that can shuttle between the cytosol and the membrane, but only when they bind to the membrane can adoperate the conversion.

When the free enzymes shuttle from the cytosol to the membrane they can bind to the molecules present in the membrane, in particular  $E_A$  binds with A and  $E_B$  binds with B. The enzymes in their bound state are indicated with  $E_A^*, E_B^*$ , they can diffuse on the membrane and act as catalysts to convert molecules of one type into molecules of the other type. In particular  $E_A^*$  catalyzes the conversion of B into A, while  $E_B^*$  catalyzes the conversion of A into B. The two membrane-bound species A and B are free to diffuse on the membrane.

Diffusion in cytosol, and diffusive shuttling process from cytosol to the membrane is assumed to be much faster than lateral diffusion on the membrane, therefore enzymes in the cytosol reach their steady state concentration much faster than the membrane-bound species. As a result of such assumption, infinite cytosolic diffusion is adopted.

The detailed list of all the reactions, prescribed by the model are indicated in Table 5.1. The reactions 1, 3, 5 (Table 5.1) compose the autocatalytic feedback loop for B, while the reactions 2, 4, 6 compose the autocatalytic feedback loop for A. The model can be alternatively seen as a competing model where the the actors are the autocatalytic feedback loop for A and B. The model is pictorially described in Fig. 5.1.

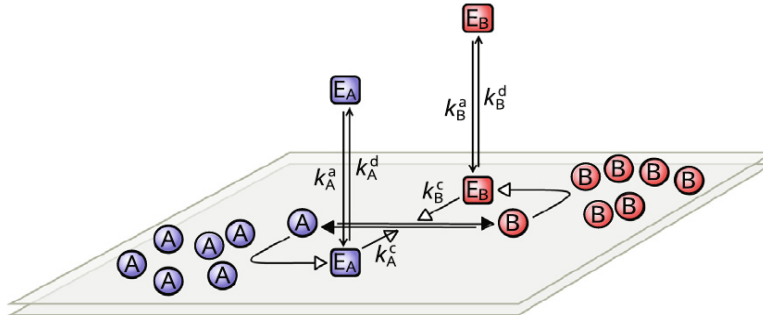


**Figure 5.1.** Representation of the model describing A-B conversion on the membrane. Ref [4]

Such model is similar to that one described in Ref. [6], there it described cell polarization due to chemotaxis: only one feedback loop was present, only membrane-bound species could diffuse, and receptors were needed to mimics the external field of chemical attractant.

With respect to such model, the proposed one present some modifications:

- Diffusion has been extended also to the bound enzymes.
- Receptors have been removed, and will be eventually inserted to study homogeneous nucleation. However the will not be called receptors but binding sites (BS).
- The model has been fully symmetrized: both the enzymes can bind to the respective membrane species and receptors (eventually).

We choose to start from the model in Ref. [6], because it was clear that such model gave phase separation in the case of homogeneous nucleation, that was possible due to receptors presence. The role of the receptors was that one of transducing an external field of chemical attractant into an internal distribution of activated enzyme catalyzing the conversion of a molecule of one type into a molecule of the other type. Therefore the phase separation was driven by an external chemical field.

In the present work, phase separation on membranes is studied in the absence of an external field, in the case of homogeneous and heterogeneous nucleation. The introduction of binding sites will not refer to the presence of an external field, but it will trigger homogeneous nucleation generating fluctuations in the number of molecules of bound enzymes.

To investigate the *phenomenology and the physics* of our model, and compare it to the one of the classical phase separation, a stochastic model simulating the reactions in Table 5.1 has been developed. Depending on the kind of nucleation that will be investigated, different sets of reactions will be simulated (further details in Table 5.1, 6.1)

The reactions are stochastically implemented via a Gillespie algorithm, and are simulated on a spherical surface lattice representing the cell membrane [7, 15]. The radius of the sphere is  $R_s = 10\mu m$ , and its surface is divided into 40950 hexagons and 12 pentagons, each polygon (face or lattice-site) can be occupied by integer amounts of membrane-bound molecule (A, B,  $E_B^*$ ,  $E_A^*$ ), representing their concentration on that particular site (Fig. 5.2).

Reactions	Type of reactions	Rate constants/Diffusivity
a. $E_B^*(i) \rightarrow S_B(i) + E_B$	Dissociation	$k_{b,s,B}^d$
b. $E_A^*(i) \rightarrow S_A(i) + E_A$	Dissociation	$k_{b,s,A}^d$
1. $E_B^*(i) \rightarrow B(i) + E_B$	Dissociation	$k_B^d$
2. $E_A^*(i) \rightarrow A(i) + E_A$	Dissociation	$k_A^d$
3. $B(i) + E_B \rightarrow E_B^*(i)$	Association	$k_B^a$
4. $A(i) + E_A \rightarrow E_A^*(i)$	Association	$k_A^a$
5. $A(i) \rightarrow B(i)$	Enzymatic mediated by $E_B^*$	$k_B^c, K_{m,B}$
6. $B(i) \rightarrow A(i)$	Enzymatic mediated by $E_A^*$	$k_A^c, K_{m,A}$
7. $A(i) \rightarrow A(j)$	Diffusive	$D$
8. $B(i) \rightarrow B(j)$	Diffusive	$D$
9. $E_A^*(i) \rightarrow E_A^*(j)$	Diffusive	$D$
10. $E_B^*(i) \rightarrow E_B^*(j)$	Diffusive	$D$

**Table 5.1.** Reactions composing the biochemical network that will be simulated by the Gillespie algorithm. The first two reactions labeled with letters are considered only in the case of homogeneous nucleation, and are simulated with the ones labeled by numbers ( $S_B$  and  $S_A$  are the binding sites for  $B$  and  $A$  respectively). On the other hand, in the case of heterogeneous nucleation only the reactions labeled with numbers will be simulated. All the types, rate constants, and diffusivity are specified. The index  $i$  denotes that the reactant is on the membrane in a specific site  $i$ , while its absence denotes the reactant is in the cytosol.

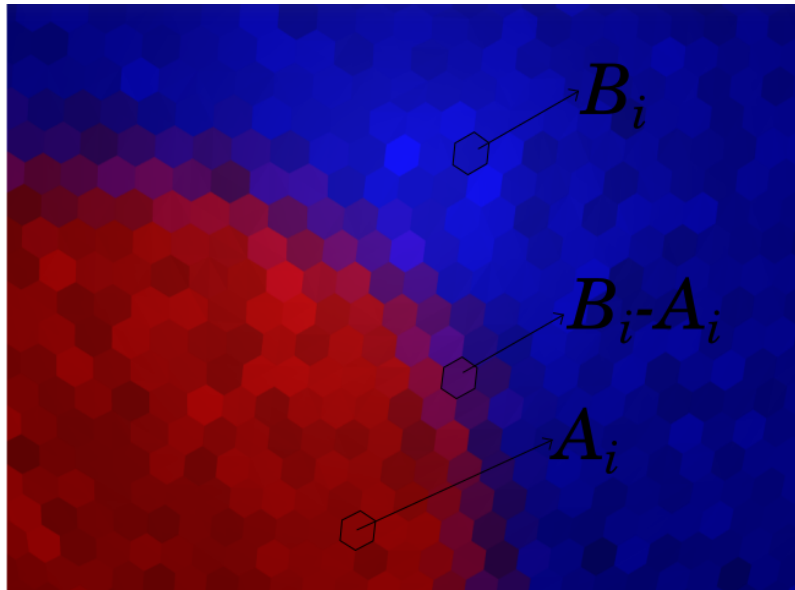


**Figure 5.2.** Portion of spherical surface divided into polygons (mostly hexagons). Each face can be occupied by an integer amount of species. In particular the upper blue face contains mostly the  $B$  molecules, the red lower one mostly the  $A$  molecules, and that one in the middle both types.

## 5.2 Mass action kinetics

In this section chemical reactions (1 to 10) of Table 5.1, will be translated in a system of differential equation, using *mass-action kinetics approach*. After that, the difference in concentration of the membrane-bound species will be rewritten in terms of an *effective free energy*, that will allow us to derive in the next section a coarse-grained description of the system.

Reaction-diffusion equations are translated in the following differential equations for the concentration of the species:

$$\frac{\partial E_B}{\partial t} = k_B^d E_B^* - k_B^a E_B B \quad (5.1)$$

$$\frac{\partial E_A}{\partial t} = k_A^d E_A^* - k_A^a E_A A \quad (5.2)$$

$$\frac{\partial E_B^*}{\partial t} = D \Delta E_B^* + k_B^a E_B B - k_B^d E_B^* \quad (5.3)$$

$$\frac{\partial E_A^*}{\partial t} = D \Delta E_A^* + k_A^a E_A A - k_A^d E_A^* \quad (5.4)$$

$$\frac{\partial B}{\partial t} = D \Delta B + g(A, B, E_A^*, E_B^*) \quad (5.5)$$

$$\frac{\partial A}{\partial t} = D \Delta A - g(A, B, E_A^*, E_B^*) \quad (5.6)$$

$$g(A, B, E_A^*, E_B^*) = k_B^c \frac{A E_B^*}{K_{m,A} + A} - k_A^c \frac{B E_A^*}{K_{m,B} + B} \quad (5.7)$$

Where  $\Delta$  is the Laplace-Beltrami operator on the curved membrane surface,  $g$  is the reaction term describing the enzyme-driven mutual conversion of A and B,  $D$  is the diffusivity that is assumed to be the same for all the diffusive species. This assumption is supported by the fact that enzymes in the cytosol diffuse much faster than membrane-bound species, however when they bind with molecules on the membrane, they start diffusing at the same velocity of the membrane-bound molecules.

If  $A + B$  is uniformly distributed at initial time, summing (5.5) and (5.6), the following conservation law remains valid for all times:

$$A + B = c$$

Subtracting Eq. 5.5 to Eq. 5.6:

$$\frac{\partial \varphi}{\partial t} = D \Delta \varphi - 2g(\varphi) \quad (5.8)$$

$$\text{where } \varphi = A - B$$

Recalling that enzymes in the cytosol reach their equilibrium concentration much faster than membrane-bound species, from (5.2) and (5.3):

$$\begin{aligned} E_B^* &= \frac{k_B^a}{k_B^d} E_B B = \frac{E_B(c - \varphi)}{2K_B^d} \\ E_A^* &= \frac{k_A^a}{k_A^d} E_A A = \frac{E_A(c + \varphi)}{2K_A^d} \\ \text{where } K_A^d &= \frac{k_A^d}{k_A^a}, \quad K_B^d = \frac{k_B^d}{k_B^a} \end{aligned}$$

Therefore:

$$\begin{aligned} -2g(\varphi) &= f_{\alpha,\beta}(\varphi) \\ &= -(c^2 - \varphi^2)[\beta h(\varphi) - \alpha h(-\varphi)] \end{aligned}$$

$$\begin{aligned} \text{where} \quad \beta &= \frac{k_B^c E_B}{K_B^d}, \quad \alpha = \frac{k_A^c E_A}{K_A^d} \\ h(\varphi) &= \frac{1}{2K_m + c + \varphi} \\ \text{assuming} \quad K_{m,A} &= K_{m,B} = K_m \end{aligned}$$

Eq. 5.8 becomes:

$$\frac{\partial \varphi}{\partial t} = D\Delta\varphi + f_{\alpha,\beta}(\varphi) \quad (5.9)$$

### 5.3 Landau-Ginzburg dynamics

In this section we want to derive a *coarse-grained* (or *phase-field*) description, of our model, in order to analytically derive in the following chapters some analytical results.

First of all, we need to make some assumptions about the biophysical system we are investigating:

- I. The state of the system can be fully described in terms of a single-component *order parameter*  $\varphi$ , which is a field describing the distribution of the membrane-bound species A, B.

$$\varphi(\mathbf{r}, t) = A(\mathbf{r}, t) - B(\mathbf{r}, t)$$

- II. The network of chemical reactions allows the realization of two distinct and locally stable phases (*Bistability*).
- III. The *metastability degree*  $\psi$  of the system is controlled by the global feedback mechanism arising from the chemical network (i.e rate constants). It controls the conversion of the two phases, and drives the system toward an equilibrium configuration characterized by phase coexistence.
- IV. The order parameter  $\varphi$  has no local constraints (*non-conserved field*).

Given the properties stated above, we adopt the *time-dependent Landau-Ginzburg model* (Eq 5.10), to study the order parameter ( $\varphi$ ) dynamics. In this way a coarse-grained description of the model in terms of the field  $\varphi$  is obtained.

Eq. 5.8 can be rewritten in variational form in terms of *effective free energy*:

$$\frac{\partial \varphi}{\partial t} = -\frac{\delta \mathcal{F}_{\alpha,\beta}}{\delta \varphi} \quad (5.10)$$

$$\text{where} \quad \mathcal{F}_{\alpha,\beta} = \int_S \left[ \frac{D}{2} |\nabla \varphi|^2 + V_\psi(\varphi) \right] d\mathbf{r} \quad (5.11)$$

$S$  is a *spherical surface* mimicking the cell membrane.  $V_\psi(\varphi)$  is an effective potential, depending on some constants of the biochemical reactions determining the degree of metastability ( $\psi$ ), which says how much is advantageous converting a region of a certain phase into a region of the other phase. Property III implies that  $\psi$  decreases when the system approaches the equilibrium, since the two phases coexist in that situation. Therefore,  $\psi$  is a decreasing function of time, and is assumed to be:

$$\psi = \psi_{\text{eq}} + A \left[ \int_S \varphi(\mathbf{r}, t) d\mathbf{r} - \int_S \varphi(\mathbf{r}, \infty) d\mathbf{r} \right] \quad (5.12)$$

Where  $\psi_{\text{eq}}$  is the equilibrium values of  $\psi$  when equilibrium is reached, while the other term shows that the approach to the equilibrium depends on the difference of the areas occupied by the phases. From (5.9, 5.10, 5.11):

$$\begin{aligned} V_\psi(\varphi) &= -\int f_{\alpha,\beta}(\varphi)d\varphi \\ &= \int (c^2 - \varphi^2)[\beta h(\varphi) - \alpha h(-\varphi)]d\varphi \end{aligned} \quad (5.13)$$

Which can be written explicitly using:

$$\int \frac{(c^2 - \varphi^2)}{2K_m + c \pm \varphi} d\varphi = \mp \frac{\varphi^2}{2} + (2K_m + c)\varphi \mp 4K_m(K_m + c)\log(2K_m + c \pm \varphi)$$

Eq. 5.13 becomes:

$$\begin{aligned} V_\psi(\varphi) &= -(\alpha + \beta)\frac{\varphi^2}{2} + (\beta - \alpha)(2K_m + c)\varphi + \\ &\quad -4K_m(K_m + c)[\beta \cdot \log(2K_m + c + \varphi) + \alpha \cdot \log(2K_m + c - \varphi)] \end{aligned} \quad (5.14)$$

$V_\psi(\varphi)$  presents two minima and one maximum. The relative and absolute minima represent respectively the metastable and stable phases.

### 5.3.1 Time evolution of a circular domain

In this section, the growth of a *circular domain* will be studied in the Landau-Ginzburg framework. In particular a differential equation describing time evolution of the radius of a circular domain will be found and solved under certain conditions.

Assuming a circular shape for a generic domain of a certain phase,  $\varphi$  can be written:

$$\varphi(\mathbf{r}, t) = \phi(R - r(t)) \quad (5.15)$$

Inserting this equation in (5.10, 5.11):

$$-\phi' \dot{R} = -\frac{\delta \mathcal{F}_\psi}{\delta \phi} \quad (5.16)$$

$$\begin{aligned} \mathcal{F}_\psi[\phi] &= \frac{D}{2} \int_0^{2\pi} d\theta \int_0^R r(\phi')^2 dr + \int_S V_\psi(\phi(R - r(t))) d\mathbf{r} \\ &\simeq \frac{D}{2} 2\pi R \gamma + \Delta V_{A,B} \int_S d\mathbf{r} \\ &= 2\pi R \sigma - \pi R^2 \psi \end{aligned} \quad (5.17)$$

Having imposed:

$$\gamma = \int_0^R (\phi')^2 dr \quad (5.18)$$

$$\sigma = \frac{D}{2} \gamma \quad (5.19)$$

$$\Delta V_{A,B} = -\psi \quad (5.20)$$

Where in (5.17) we have used the thin-wall approximation:  $R$ ,  $V_\psi(\phi)$  can be considered constant over the small interface (thin-wall) between the phases.

Multiplying both sides of Eq. 5.16 by  $\phi'$ , and integrating over the surface:

$$\begin{aligned} -\dot{R} \int_S (\phi')^2 d\mathbf{r} &= - \int_S \frac{\delta \mathcal{F}_\psi}{\delta \phi} \phi' d\mathbf{r} \\ &= \frac{d\mathcal{F}}{dR} \\ &= 2\pi\sigma - 2\pi R\psi - \pi R^2\psi' \end{aligned}$$

Recalling that:

$$-\dot{R} \int_S (\phi')^2 d\mathbf{r} = -2\pi R\gamma \dot{R}$$

We finally obtain:

$$\gamma \dot{R} = -\frac{\sigma}{R} + \psi + \frac{1}{2}R\psi'$$

We assume that  $\psi = \psi(\bar{\varphi})$ , reaches an equilibrium value  $\psi_{\text{eq}} = \psi(\bar{\varphi}_{\text{eq}})$ . We expand  $\psi$  around this value, assuming that the first order term is a linear function proportional to the difference between the area occupied by the phase at a certain time and the area occupied by the phase at equilibrium (mimicking (5.15)):

$$\begin{aligned} \psi &= \psi_{\text{eq}} + \frac{C}{2}(R_{\text{eq}}^2 - R^2) & (5.21) \\ \Rightarrow \psi' &= -CR \\ \Rightarrow \gamma \dot{R} &= -\frac{\sigma}{R} + \psi_{\text{eq}} + \frac{C}{2}(R_{\text{eq}}^2 - R^2) - \frac{C}{2}R^2 \end{aligned}$$

Where  $R_{\text{eq}}$  is the equilibrium radius of a domain of a certain phase. It is clear that for  $R = R_{\text{eq}}$  the domain stops growing and the equilibrium size is reached ( $\gamma \dot{R} = 0$ ):

$$\psi_{\text{eq}} = \frac{\sigma}{R_{\text{eq}}} + \frac{C}{2}R_{\text{eq}}^2 \quad (5.22)$$

$$\Rightarrow \gamma \dot{R} = \sigma \left[ \frac{1}{R_{\text{eq}}} - \frac{1}{R} + \frac{1 - (R/R_{\text{eq}})^2}{L} \right] \quad (5.23)$$

Having imposed:

$$L = \frac{CR_{\text{eq}}^2}{\sigma}$$

We assume the existence of a critical size ( $R_c$ ), on which domains growth depends. In particular, if a domain has an initial radius which is lower than  $R_c$  the domain will extinguish, while in the opposite situation the domain will grow. We also assume that this quantity increases up to  $R_{\text{eq}}$ , as time proceeds, according to what is stated in property V in the case of classical phase separation.

Therefore we are allowed to identify the r.h.s of Eq. 5.23 with a function of  $R$  and  $R_c$ , which vanish at  $R_c$ , and it's positive (and negative), above (and below)  $R_c$ :

$$\begin{aligned} \Rightarrow \gamma \dot{R} &= \sigma \left[ \frac{1}{R_{\text{eq}}} - \frac{1}{R} + \frac{1 - (R/R_{\text{eq}})^2}{L} \right] \\ &= \sigma \left[ \frac{1}{R_c} - \frac{1}{R} \right] \\ \Rightarrow R_c &= \frac{1}{\frac{1}{R_{\text{eq}}} + \frac{1 - (R/R_{\text{eq}})^2}{L}} \end{aligned}$$

$R_c$  is an increasing function of  $R$ .

In the limit of large  $R$ :

$$R_c \lesssim R_{\text{eq}}$$

While in the limit of small  $R$ :

$$\begin{aligned} R_c &\gtrsim \frac{1}{\frac{1}{R_{\text{eq}}} + \frac{1}{L}} \\ \Rightarrow R_c &\sim R_c^* \sim L \quad \text{if} \quad R, L \ll R_{\text{eq}} \end{aligned} \quad (5.24)$$

Where  $R_c^*$  is the critical size of the domain at the beginning of the process.

We have just derived the differential equation for the *radius dynamics* (5.23). Now we want to solve such equation, recalling that  $R_{\text{eq}}$  is stationary point for  $R(t)$ , because it's the maximal radius that the domain can reach. Therefore  $R_{\text{eq}}$  must be a root of the r.h.s of Eq. 5.23.

(5.23) becomes:

$$\frac{\gamma}{\sigma} R \dot{R} = -\frac{(R - R_{\text{eq}})}{L R_{\text{eq}}^2} [R^2 + R R_{\text{eq}} - L R_{\text{eq}}]$$

Now let's focus on finding the other two roots of the expression in squared brackets:

$$R_1, R_2 = \frac{-R_{\text{eq}} \pm \sqrt{R_{\text{eq}}^2 + 4R_{\text{eq}}L}}{2} \quad (5.25)$$

where  $R_1 < 0, R_2 > 0$

$$\begin{aligned} \Rightarrow \frac{\gamma}{\sigma} R \dot{R} &= -\frac{(R - R_{\text{eq}})(R - R_1)(R - R_2)}{L R_{\text{eq}}^2} \\ \Rightarrow \int_{R_0}^R \frac{R'}{(R' - R_{\text{eq}})(R' - R_1)(R' - R_2)} dR' &= -\frac{\sigma}{\gamma L R_{\text{eq}}^2} \int_{t_0}^t dt' \\ \Rightarrow -\frac{\sigma}{\gamma L R_{\text{eq}}^2} (t - t_0) &= I(R, R_0) \end{aligned} \quad (5.26)$$

The integral can be solved analytically using fractal decomposition:

$$I(R, R_0) = \int_{R_0}^R \left( \frac{A}{R' - R_{\text{eq}}} + \frac{B}{R' - R_1} + \frac{C}{R' - R_2} \right) dR' \quad (5.27)$$

$$\begin{aligned} &= \frac{R_{\text{eq}}}{(R_{\text{eq}} - R_1)(R_{\text{eq}} - R_2)} \cdot \log \left| \frac{R - R_{\text{eq}}}{R_0 - R_{\text{eq}}} \right| + \frac{R_1}{(R_1 - R_{\text{eq}})(R_1 - R_2)} \cdot \log \left| \frac{R - R_1}{R_0 - R_1} \right| + \\ &+ \frac{R_2}{(R_2 - R_{\text{eq}})(R_2 - R_1)} \cdot \log \left| \frac{R - R_2}{R_0 - R_2} \right| \end{aligned} \quad (5.28)$$

$$= f(R, R_0, R_1, R_2, R_{\text{eq}}) \quad (5.29)$$

The initial critical radius  $R_c^*$  must be a root too, because it's the minimal radius that domain must have in order to grow, therefore it must be the positive one:

$$R_c^* = R_2 \quad (5.30)$$

$$\Rightarrow L = R_c^* + \frac{(R_c^*)^2}{R_{\text{eq}}} \quad (5.31)$$

Therefore, recalling (5.19), Eq. 5.26 becomes:

$$t = t_0 - \frac{DLR_{\text{eq}}^2}{2} \cdot f(R, R_0, R_{\text{eq}}, L) \quad (5.32)$$

We have finally obtained an equation describing how the radius of a domain evolves through time, knowing a set of parameters:  $D, R_{\text{eq}}, R_0, L$ .

Since stochastic simulations will provide the behavior of a single domain radius over time, we will compare it to the theoretical one.

### 5.3.2 Structure of the phase boundary

In this section we are going to solve Eq. 5.9, in the particular case in which  $V_\psi$  has the following form:

$$V_\psi(\varphi) = b(c^2 - \varphi^2)^2, \quad b > 0 \quad (5.33)$$

This potential has two symmetric minima in  $\varphi = \pm c$ , and a single maximum in  $\varphi = 0$ . The term  $bc^4$  quantifies the distance between the minimum and the maximum and the minimum. Therefore such potential resembles the qualitative feature of the original one (5.13), keeping in mind that  $b$  is linked to the constants in (5.13).

Finally we will use the solution of (5.9) to define the *width* of the interface separating two distinct phases, and understand how it's linked to the fundamental parameters of the model.

The field  $\varphi$ , will be a stationary front depending only on the radial coordinate:

$$\begin{aligned} \varphi(\mathbf{r}, t) &= \phi(R - r(t)) \\ \text{defining } R - r(t) &= \xi(t) \end{aligned}$$

Inserting (5.15) into (5.9), we obtain:

$$-\dot{r}(t) \frac{\partial \phi}{\partial \xi} = D \left[ \frac{1}{R} \frac{\partial \phi}{\partial \xi} + \frac{\partial^2 \phi}{\partial \xi^2} \right] + f_{\alpha, \beta}(\phi)$$

Where we have written the Laplace-Beltrami operator on a plane in polar coordinates.

Looking for a stationary front ( $\dot{r}(t) = 0$ ), and recalling (5.13):

$$\begin{aligned} \Rightarrow D \left[ \frac{1}{R} \frac{\partial \phi}{\partial \xi} + \frac{\partial^2 \phi}{\partial \xi^2} \right] &= -f_{\alpha, \beta}(\phi) \\ &= \frac{\partial V_\psi}{\partial \phi} \\ &= \frac{\partial V_\psi}{\partial \xi} \frac{\partial \xi}{\partial \phi} \\ \Rightarrow \frac{\partial}{\partial \xi} \left[ \frac{D}{2} (\phi')^2 - b(c^2 - \phi^2)^2 \right] &= 0 \\ \Rightarrow \frac{D}{2} (\phi')^2 - b(c^2 - \phi^2)^2 &= C \\ &= 0 \\ \text{where } \phi' &= \frac{\partial \phi}{\partial \xi} \end{aligned} \quad (5.34)$$

Where the term inversely proportional to  $R$  has been neglected, Eq. 5.33 has been used, and  $C = 0$  because  $\phi(\pm\infty) = \pm 1$ , and  $\phi'(\pm\infty) = 0$ .

Eq. 5.34 becomes:

$$\sqrt{\frac{D}{2b}}(\phi') = (c^2 - \phi^2)$$

Such differential equation is easily integrated:

$$\begin{aligned}\phi &= c \cdot \tanh\left(c\sqrt{\frac{2b}{D}}(\xi - \xi_0)\right) + \text{cost} \\ &= c \cdot \tanh\left(\frac{\xi - \xi_0}{\delta}\right) + \text{cost}\end{aligned}\quad (5.35)$$

Where the width of the interface between the two phase has been defined:

$$\begin{aligned}\delta &= \sqrt{\frac{D}{2bc^2}} = h\sqrt{D} \\ \text{where } h &= \frac{1}{c\sqrt{2b}}\end{aligned}\quad (5.36)$$

We notice that the width increases as diffusion increases, while decreases if  $b$  decreases. This means that a potential featuring a shorter energy gap between maximum and relative minimum ( $bc^4$ ), will lead to a larger interface.

### 5.3.3 Interfacial tension

In this section we are going to solve Eq. 5.18, in the case of a particular form of  $\phi$ . Then we will use the solution to write an explicit expression for  $\sigma$ , underlining its dependence on fundamental parameters.

The form of  $\phi$  is similar to that one in (5.35), however it has been generalized to allow the function to have different asymptotic values:

$$\phi = \bar{A} - \bar{B} \cdot \tanh\left(\frac{R - R_{\text{eq}}}{\delta}\right)\quad (5.37)$$

Where  $\bar{A}$  and  $\bar{B}$  are such that:

$$\begin{aligned}\bar{A} + \bar{B} &= \langle A \rangle \\ \bar{A} - \bar{B} &= \langle B \rangle\end{aligned}$$

Being  $\langle A \rangle, \langle B \rangle$  the mean values of the phase A and B in the regions where they are abundant.

Eq. 5.18 becomes:

$$\begin{aligned}\gamma &= \int_0^\infty \frac{\bar{B}^2}{\delta^2} \cdot \text{sech}^4(R - R_{\text{eq}}) dR \\ &= \frac{\bar{B}^2}{3\delta} g(R_{\text{eq}}, \delta) \\ \text{where } g(R_{\text{eq}}, \delta) &= 2 - \tanh\left(\frac{R_{\text{eq}}}{\delta}\right) \cdot \left[ \tanh^2\left(\frac{R_{\text{eq}}}{\delta}\right) - 3 \right] \simeq 4 \\ \Rightarrow \gamma &\simeq \frac{4\bar{B}^2}{3\delta}\end{aligned}\quad (5.38)$$

Recalling (5.19, 5.36) we can now derive the expression for  $\sigma$ :

$$\sigma = \gamma \frac{D}{2} = \frac{2\bar{B}^2}{3h} \sqrt{D} \quad (5.39)$$

Which depends on:

- The steady state value of the phase B concentration ( $\bar{B}$ ).
- Diffusivity ( $D$ )
- The potential barrier ( $b$  depending on  $h$ )

Deriving numerical values for  $\bar{B}$  and  $\delta$ , from numerical simulations, we are going to find a numerical estimation of  $\sigma$ . After that we will study its dependency on diffusivity  $D$ .



# Chapter 6

## Numerical results

Our objective is to demonstrate that our model is able to capture the phenomenology and the physics of phase separation on membranes. Therefore, in this chapter, we will show which kind of simulations are performed and how the emerged membrane-bound concentration dynamics reproduce the same phenomenology of classical phase separation (Sec 6.2.1). Moreover, the behavior of fundamental parameters, will be simulated and compared to the theoretical ones.

### 6.1 Simulation protocol

The system was prepared at initial time assigning the total number of enzymes in the cytosolic compartment, and populating each lattice site with B molecules, except for localized regions specified below. The system was run with zero diffusivity until the enzyme distribution between cytosol and membrane equilibrated. The system was simulated with three different purposes:

1. Study concentration dynamics of membrane-bound species in the case of homogeneous nucleation
2. Study concentration dynamics of membrane-bound species in the case of heterogeneous nucleation
3. Study the physics of a single growing domain

In the first case all the reactions in Table 5.1 are simulated, since the presence of the first two reactions triggers homogeneous nucleation of one of the two phases in the situation in which the initial configuration prescribes the presence of a unique phase.

In the second case only reactions 1 to 10 of Table 5.1 are simulated, since heterogeneous nucleation will be simulated using an initial configuration prescribing the presence of some small domains of phase A immersed in a sea of the phase B, therefore the first two reactions will not be used.

In the last case, the simulated reactions are the same of case 2, however the initial configuration prescribes the presence of a single domain, whose growth is studied. For the present simulations the parameters are tuned in such a way that initial domains of phase A which are smaller than a certain size evaporate, while the larger ones survive. We denote such threshold size as the radius ( $R_c^*$ ) of a circular domain having the same area of the extinguished initial domain. The parameters for case 3 in Table 6.1, provide a critical size  $R_c^* \sim 1$ .

Parameters values	Case 1	Case 2	Case 3	Units
$k_{b,s,B}^d$	50	/	/	$s^{-1}$
$k_{b,s,A}^d$	50	/	/	$s^{-1}$
$k_B^d$	1	1	1	$s^{-1}$
$k_A^d$	1	1	1	$s^{-1}$
$k_B^a$	10	10	1	$\mu M^{-1} s^{-1}$
$k_A^a$	10	10	1	$\mu M^{-1} s^{-1}$
$k_B^c$	1	1	0.1	$s^{-1}$
$k_A^c$	0.1	0.1	0.01	$s^{-1}$
$K_{m,B}$	0.2	0.2	0.2	$\mu M^{-1}$
$K_{m,A}$	0.2	0.2	0.2	$\mu M^{-1}$
$D$	0.002	0.005	0.001	$\mu m^2 s^{-1}$
$c$	2	2	2	$\mu M$
$E_{A,tot}$	5	5	5	$nM$
$E_{B,tot}$	5	5	16	$nM$
$S_A$	60	/	/	$nM$
$S_B$	60	/	/	$nM$

**Table 6.1.** List of parameters values used in the simulations in the three kind of simulations.

The simulation program [7, 15] can:

- Import any initial configuration, describing the amount of molecules per site, and the global amount of enzymes (see Fig. 6.1).
- Import the rate constants and diffusivity associated to the reactions.
- Export all the system configurations at a given time, describing the amount of molecules per site, and the global amount of free enzymes.

```

00000_Detailed_State_00:00:00.txt
1 1425 4062313 31987 1475 13 8525
2 0 98 2 0 0 0
3 0 99 1 0 0 0
4 0 99 1 0 0 0
5 0 98 2 0 0 0
6 0 100 0 0 0 0
7 0 100 0 0 0 0
8 0 99 1 0 0 0
9 0 99 1 0 0 0
10 0 100 0 0 0 0
11 0 100 0 0 0 0
12 0 99 1 0 0 0
13 0 100 0 0 0 0
14 0 99 1 0 0 0
15 0 97 3 0 0 0
16 23 0 0 77 0 0
17 0 99 1 0 0 0
18 0 100 0 0 0 0
19 0 99 1 0 0 0
20 0 100 0 0 0 0
21 0 98 2 0 0 0
22 0 99 1 0 0 0

```

**Figure 6.1.** Equilibrated initial state. Such initial configuration has been obtained running a simulation of a single growing domain ( $R = 1.62$ ), in absence of diffusion ( $D = 0$ ). The first line contains the total amount of molecules in the system (in order  $A, B, E_B^*, E_A^*, E_B, E_A$ ). All the other rows contain the number of the molecules per face (first 4 columns), the face is labelled by the row number.

### 6.1.1 Microscopic units

In Table 6.1, the parameters are expressed in physical units, however it is useful to understand how they are used by the program, since all the numerical results that will be shown, will be expressed in microscopic units, i.e fundamental units of the program. Such microscopic units, by which, all the quantities are rescaled are: time  $\bar{\tau}$ , and length  $d$ . The first is the characteristic time for a molecule to jump from a site to a specific nearest neighbor, with jump rate  $r_D$ . The second is the length of such jump, which is the distance between the centers of two neighboring sites.

The process by which a molecule jump from one site to one of its neighbors is the diffusion process. On a hexagonal lattice, diffusivity can be written:

$$D = \sqrt{3}r_D a$$

Where  $r_D$  is the jump rate per molecule from a site to a specific neighboring site, and  $a$  is the area of an hexagon. The area of a single hexagon can be easily computed recalling that the sphere is composed by 40962 ( $N_F$ ) faces (all hexagons for simplicity) and that the radius is  $R_s = 10\mu m$ :

$$\begin{aligned} a N_F &\simeq 4\pi R_s^2 \\ \Rightarrow a &\simeq \frac{4}{N_F}\pi R_s^2 \sim 3.066 \cdot 10^{-2} \mu m^2 \end{aligned} \quad (6.1)$$

Since the area of a single hexagon can be written as function of the distance between two neighboring centers, one can find the expression for the microscopic units:

$$\begin{aligned} a &= \frac{\sqrt{3}}{2}d^2 \\ \Rightarrow d &= \sqrt{\frac{2a}{\sqrt{3}}} \sim 0.188\mu m \\ \Rightarrow \bar{\tau} &= \frac{1}{r_D} \end{aligned}$$

All the parameters are rescaled taking into account such microscopic units, for example, diffusivity, is translated by the program into jump rate  $r_D$  in order to perform the diffusion process.

## 6.2 Phenomenology of diffusion-controlled phase separation

### 6.2.1 Nucleation, coarsening, and relaxation to the steady state

In the present section, we are going to show spatial distribution of membrane-bound molecules on the membrane. We will simulate and visualize the dynamics of the membrane-bound species concentration in two different situations: a first one in which at the beginning there is only phase B and small domains of phase A appears by stochastic fluctuations (homogeneous nucleation), and a second one in which the initial configuration already contains a finite number of phase A domains in a sea of phase B (heterogeneous nucleation).

In both situations, we will see that as time proceeds, the number of domains reduces until only

one survives (occupied by phase A), and the complementary region is occupied by phase B. Such dynamics resembles that one prescribed by classical phase separation (Chapter 2).

### Homogeneous nucleation

As mentioned before, to trigger an homogeneous nucleation we need the presence of binding sites, therefore all the reactions in Table 5.1 are simulated using the rates shown in Table 6.1 for case 1. Visualization of field and single phases dynamics are shown below; colormap and colorbar give an indication about how many molecules are present in each site; they are shown in Fig. 6.8.

Starting from an initial configurations in which only the phase B is present, few domains of phase A appear after some time (Fig. 6.2, 6.5) and start growing. However after some time one of the three domains start to evaporate (Fig. 6.3, 6.6), while the remaining ones survive and grow.

As time proceeds, coarsening slows down (from  $t = 15\tau$  to  $t = 250\tau$ ), and the last domains that have been survived so far start to evaporate (Fig. 6.4, 6.7). Such behavior resembles that one of classical phase separation for which as time goes on, larger domains evaporate because of the continuous increase of the critical size under which the domains evaporate (see properties IV, V of classical phase separation). When the second-last domain evaporate (Fig. 6.4, 6.7 at  $t = 250\tau$  in back), the system finally relax to the steady state, which is characterized by a region occupied by a single phase separated by an other region occupied by the other phase (Fig. 6.4, 6.7 at  $t = 304\tau$ ). The region occupied by the the less stable phase (A), is circular, and a radial visualization of it is proposed in Fig. 6.9. Such field representation is very similar to that one of Fig. 2.1 in the case of classical phase separation. Circularity of the steady state domain resembles a characteristic of classical phase separation for which the perimeter length between two phases tend to be minimized, due to the presence of a interfacial tension.

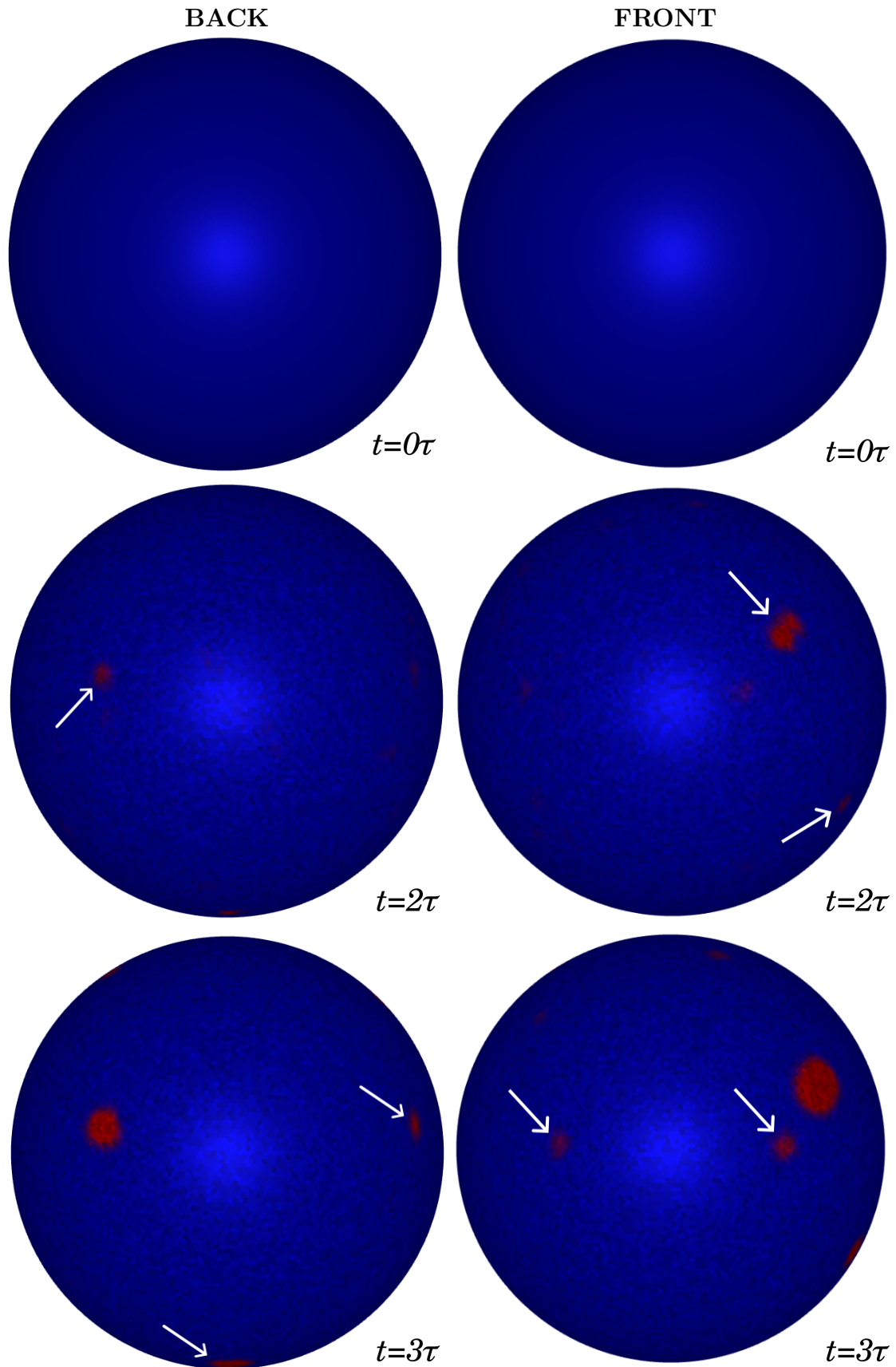


**Figure 6.2.** Homogeneous nucleation. Domains of phase A (red) spontaneously generate in the sea of B phase (blue). The initial configuration ( $t=0\tau$ ), prescribes the presence of the phase B only (back and front). At  $t=2\tau$  and  $t=3\tau$ , stochastic fluctuations of phase A induce domains nucleation (white arrows). The single phases are visualized in two different color channels (red for A, blue for B) at each time-step  $\tau$ , according to colormap in Fig. 6.8.

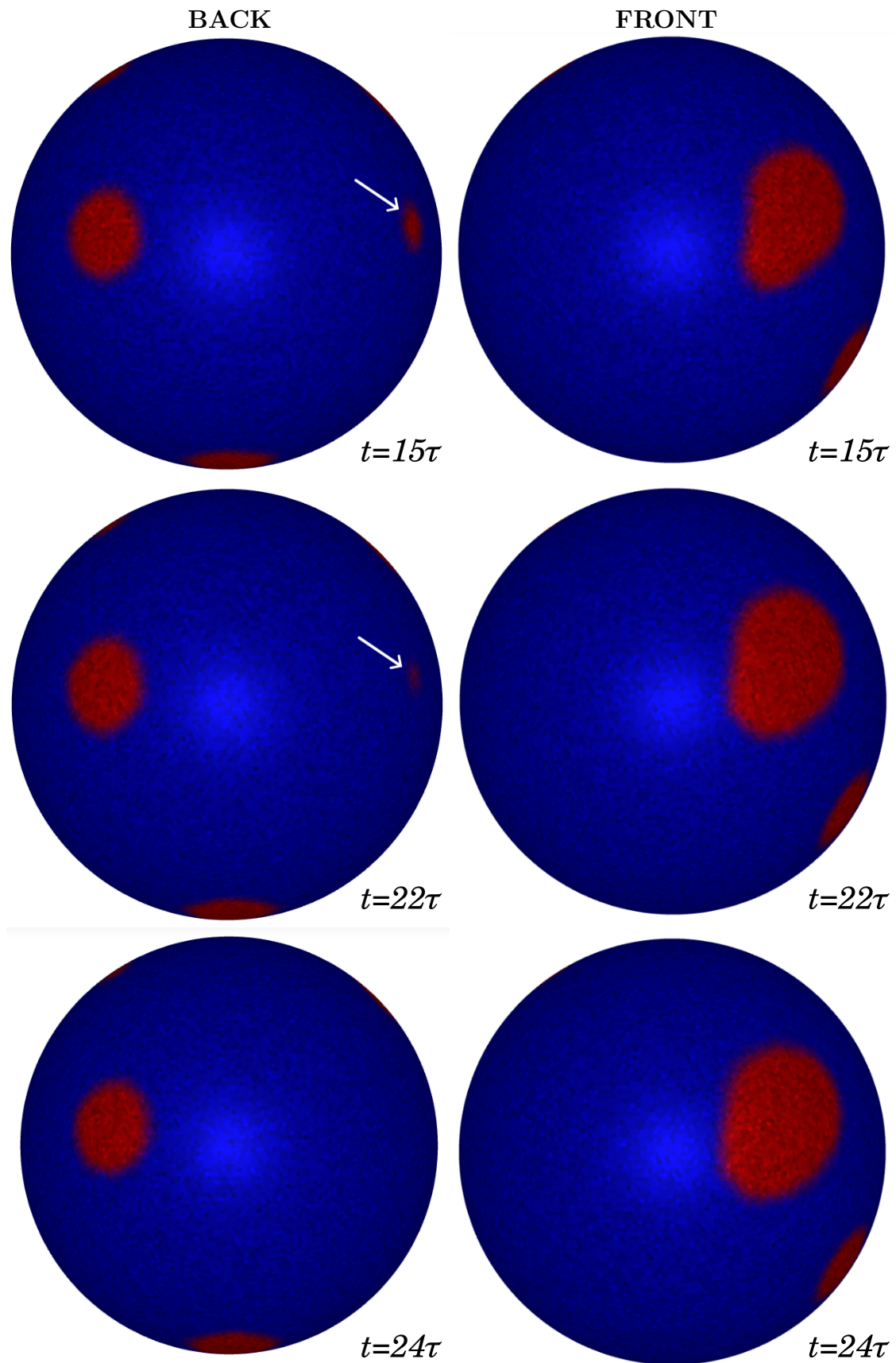


**Figure 6.3.** Early coarsening. As result of competition between phase A domains, the red one on the right evaporates (white arrow in back), while the remaining ones survive and grow. The single phases are visualized in two different color channels (red for A, blue for B) at each time-step  $\tau$ , according to colormap in Fig. 6.8.

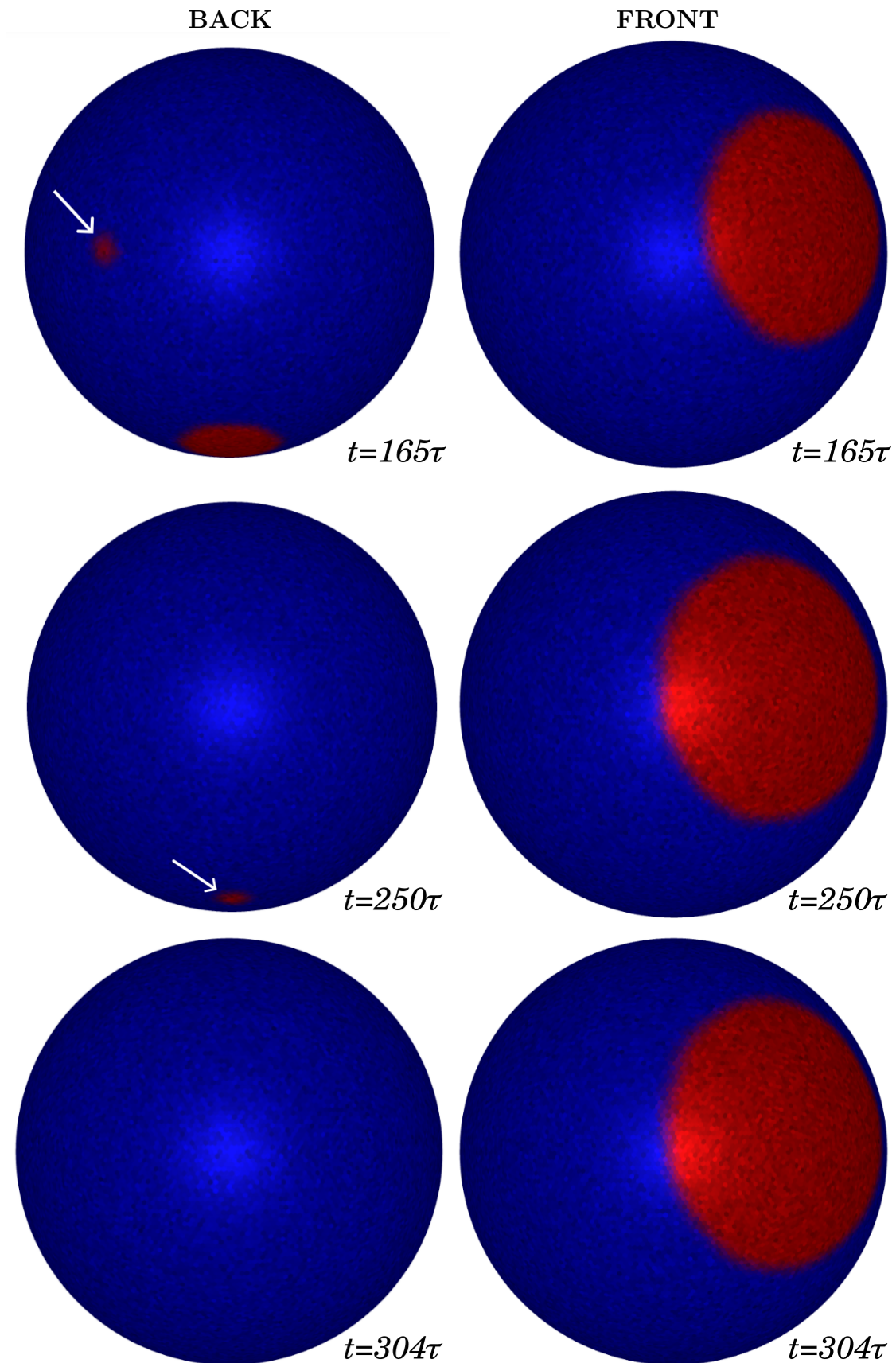


**Figure 6.4.** Late coarsening stage and relaxation to single-domain steady state. As time proceeds all the phase A domains (red) evaporates (white arrows in back), except one (in front). The last one reach an equilibrium size, and phase A a phase B coexist at equilibrium. The single phases are visualized in two different color channels (red for A, blue for B) at each time-step  $\tau$ , according to colormap in Fig. 6.8.

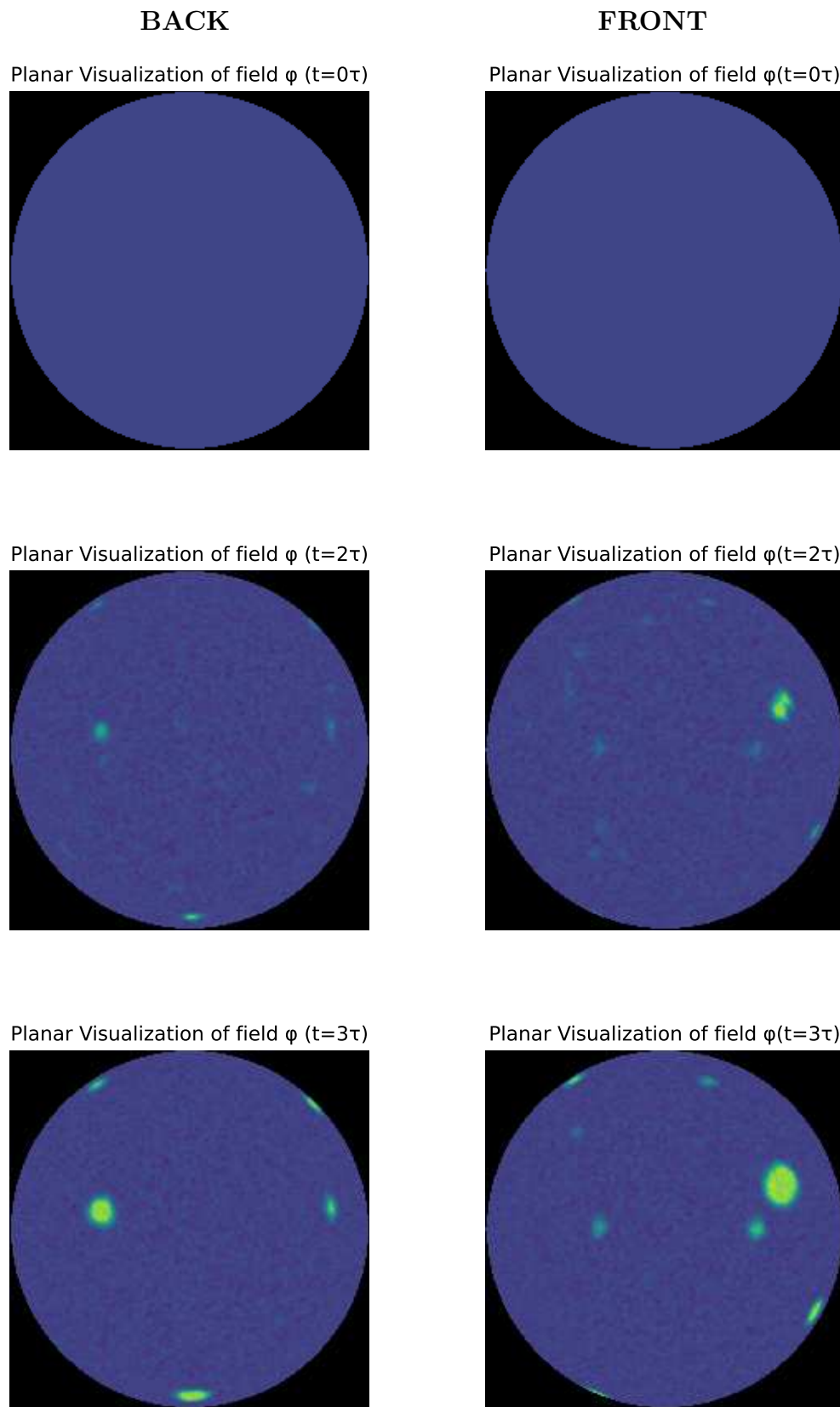


**Figure 6.5.** Homogeneous nucleation. Planar visualization of field  $\varphi$  at the same time-steps of Fig. 6.2. The yellow spots represent high values of the field, so A is abundant in the regions in which the new domains are forming, while blue “sea” represents low values of the field (phase B). Field  $\varphi$  is visualized according to colorbar in Fig. 6.8.

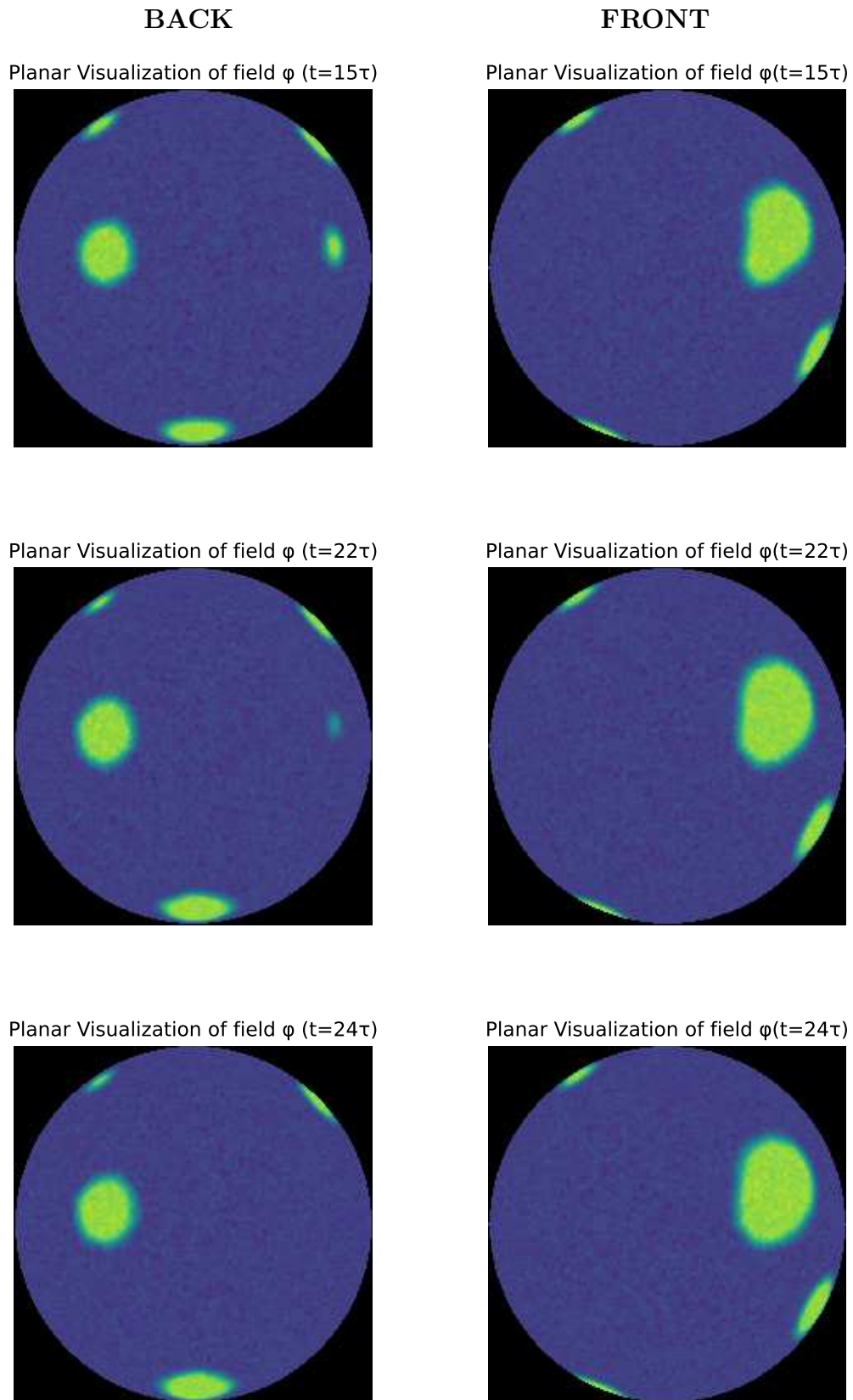


**Figure 6.6.** Early coarsening. Planar visualization of field  $\varphi$  at the same time-steps of Fig. 6.3. The yellow spots represent high values of the field, so A is abundant in the domains that survive and grow, while it assumes lower values as time proceeds in the extinguishing phase A domain on the left. Field  $\varphi$  is visualized according to colorbar in Fig. 6.8.

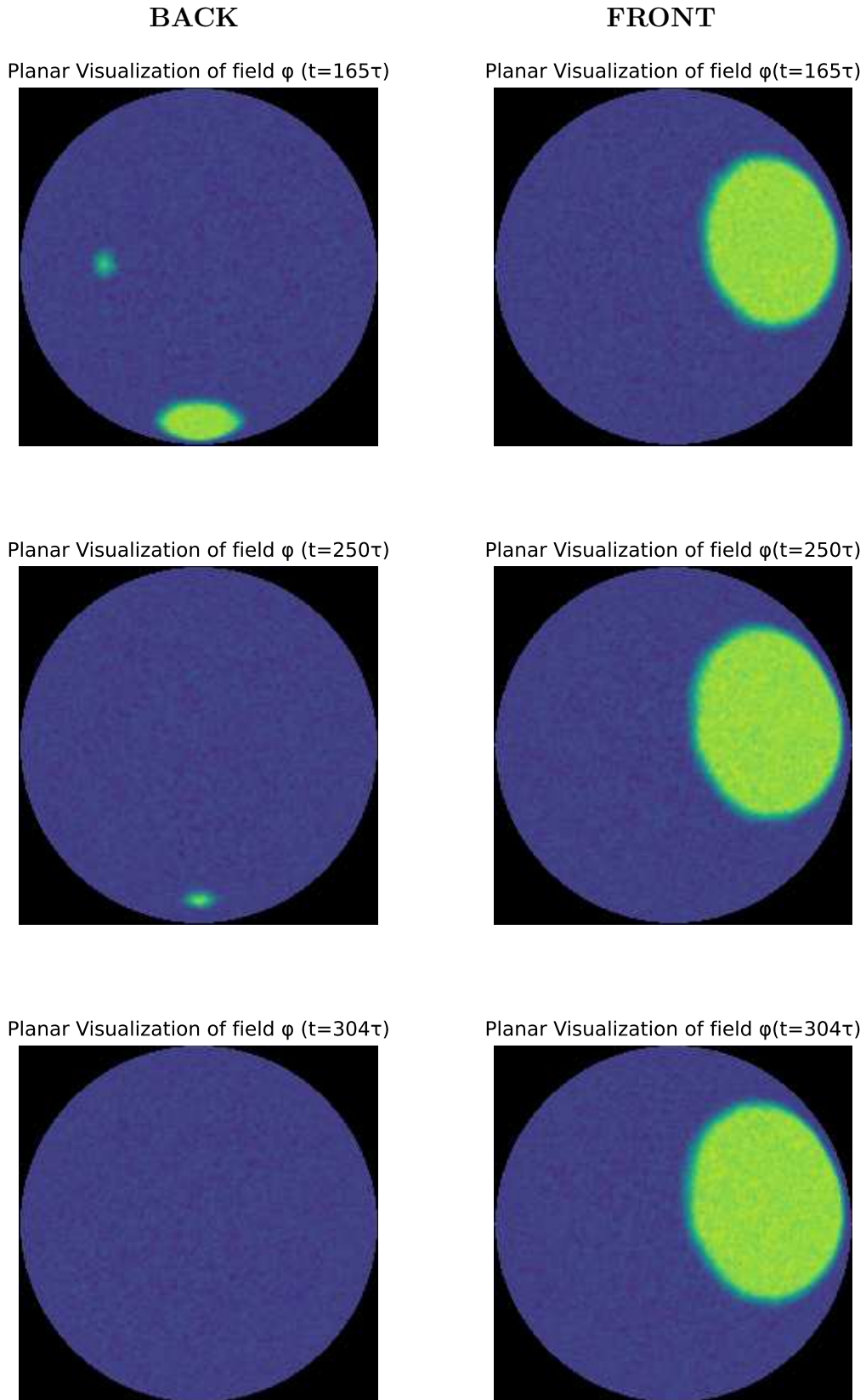


**Figure 6.7.** Late coarsening stage and relaxation to single-domain steady state. Planar visualization of field  $\varphi$  at the same time-steps of Fig. 6.4. The yellow spots represent high values of the field, so B is abundant in the regions of the vanishing domains (back), while A is abundant in the circular survived domain (front). Field  $\varphi$  is visualized according to colorbar in Fig. 6.8.

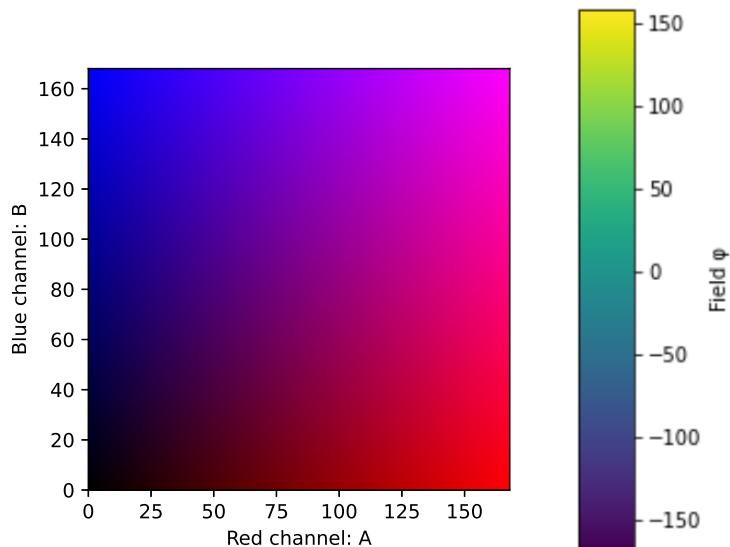


**Figure 6.8.** Color-map and color-bar. They show the relation between colors and number of molecules per site, in Fig. 6.2, 6.3, 6.4 (color-map) and Fig. 6.5, 6.6, 6.7 (color-bar).

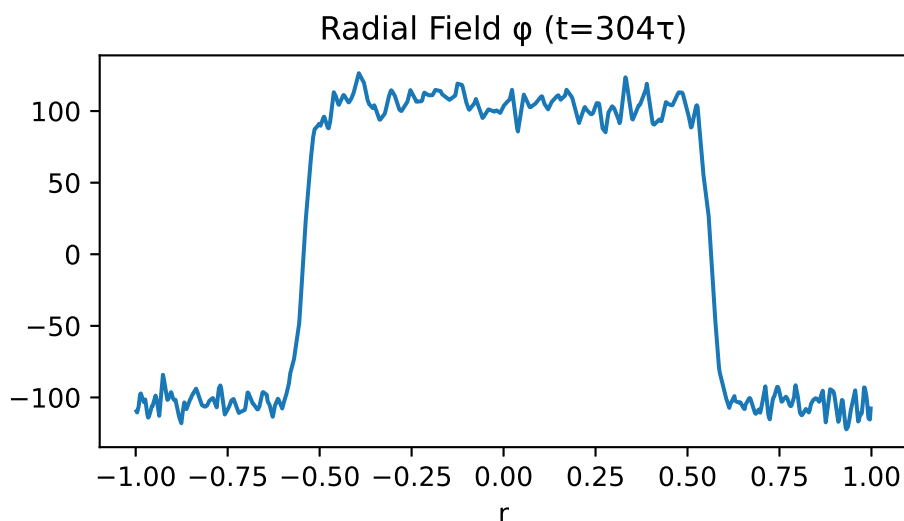


**Figure 6.9.** Radial visualization of field  $\phi$  at equilibrium ( $t=304\tau$ ), showing that the phases occupy two distinct regions of the surface.

### Heterogeneous nucleation

The same phenomenology discussed above, is observed in the case of *heterogeneous nucleation*. Reactions 1 to 10 of Table 5.1 are simulated using the rates shown in Table 6.1 for case 2, starting from an initial configuration in which multiple domains of phase A are immersed in a sea of phase B. Visualization of field and membrane-bounds dynamics are shown below; colormap and colorbar of such visualization are shown in Fig. 6.16.

Since heterogeneous nucleation has been forced by introducing that particular initial condition, we will focus on observing coarsening (Fig. 6.10, 6.11, 6.13, 6.14) and relaxation to steady state (Fig. 6.12, 6.15).

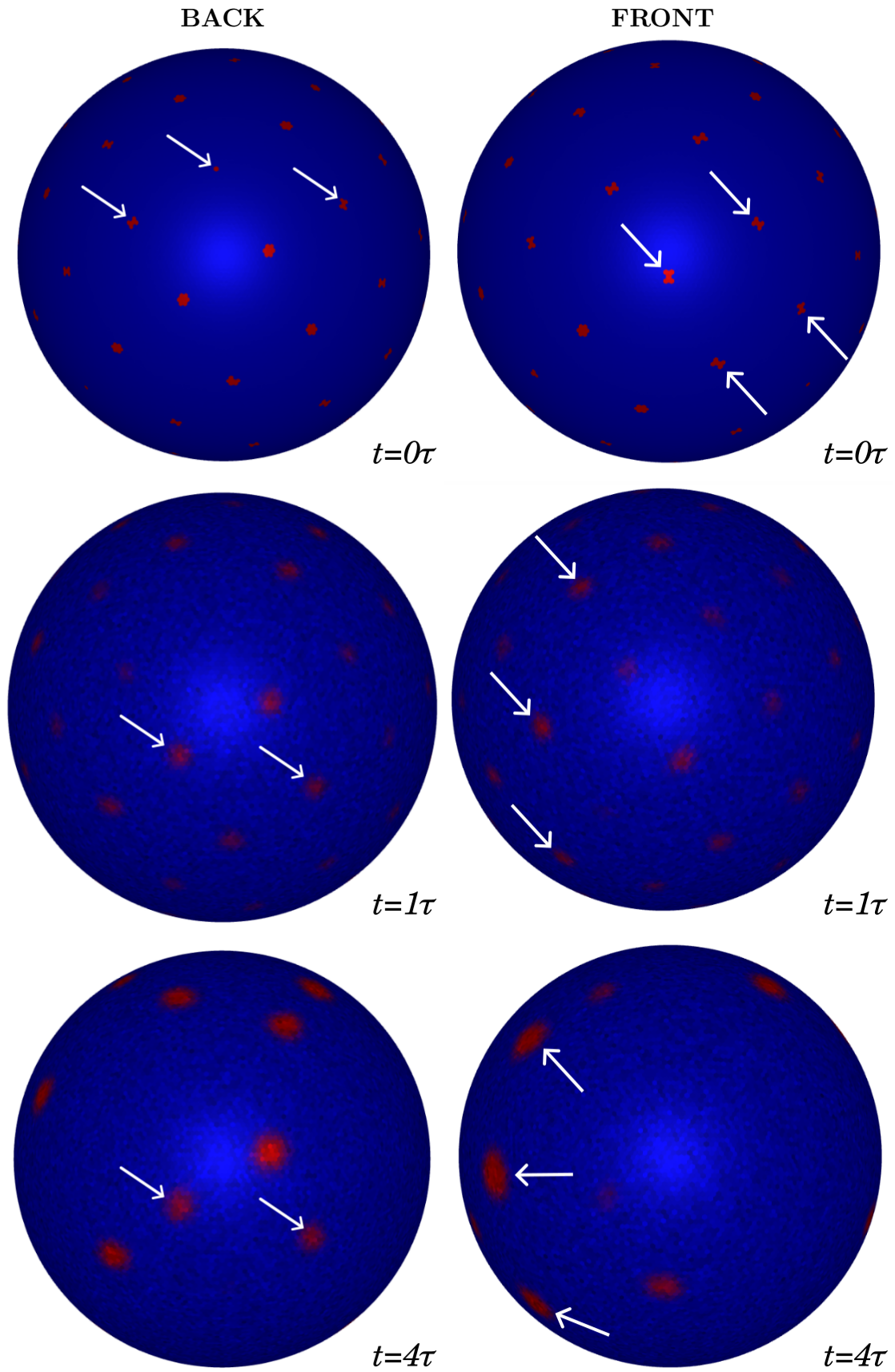


**Figure 6.10.** Heterogeneous nucleation and early coarsening stages. Domains of phase A (red) are immersed in a sea of B phase (blue) at  $t=0\tau$ . Some of the initial domains (white arrows in  $t=0\tau$ ) completely evaporate at  $t=1\tau$  and  $t=4\tau$ , while other domains survive (white arrows in  $t=1\tau$  and  $t=4\tau$ ). The single phases are visualized in two different color channels (red for A, blue for B) at each time-step  $\tau$ , according to colormap in Fig. 6.16.

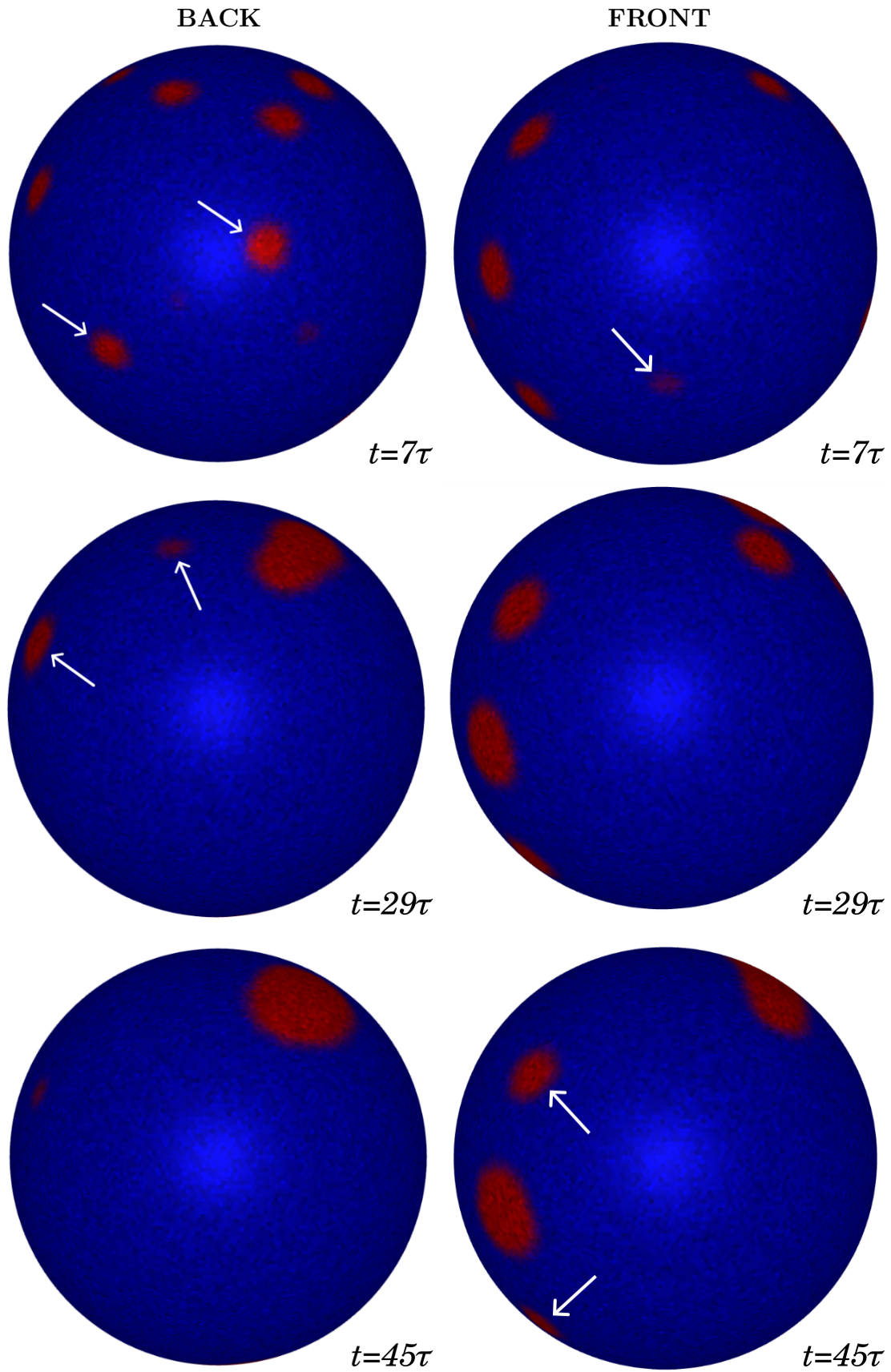


**Figure 6.11.** Coarsening stage. As result of competition between phase A domains, some of them evaporate (white arrows in back), while the remaining ones survive and grow. Domains of phase A in front at  $t=45\tau$  start to shrink, we will see them disappear in Fig. 6.12. The single phases are visualized in two different color channels (red for A, blue for B) at each time-step  $\tau$ , according to colormap in Fig. 6.16.

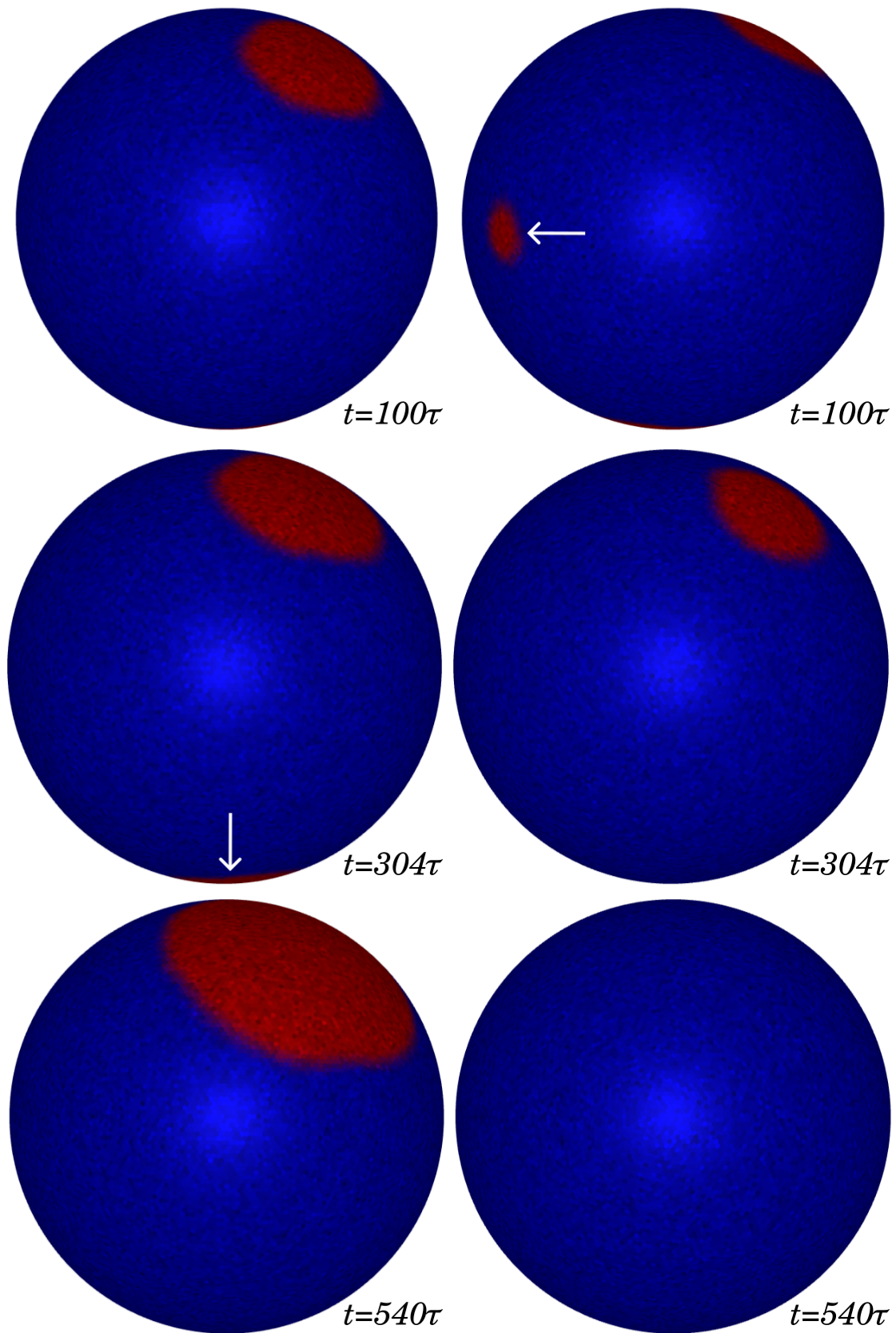


**Figure 6.12.** Late coarsening and relaxation to steady state. Domains of phase A shown at  $t = 45\tau$  completely evaporate at  $t = 540\tau$  (front), leading to a dominant phase B on the front of the sphere. On the back of the sphere only one domain of phase A survive and grows reaching an equilibrium size. From the images at  $t = 540\tau$  phase A a phase B coexist occupying two distinct regions of the surface. The single phases are visualized in two different color channels (red for A, blue for B) at each time-step  $\tau$ , according to colormap in Fig. 6.16

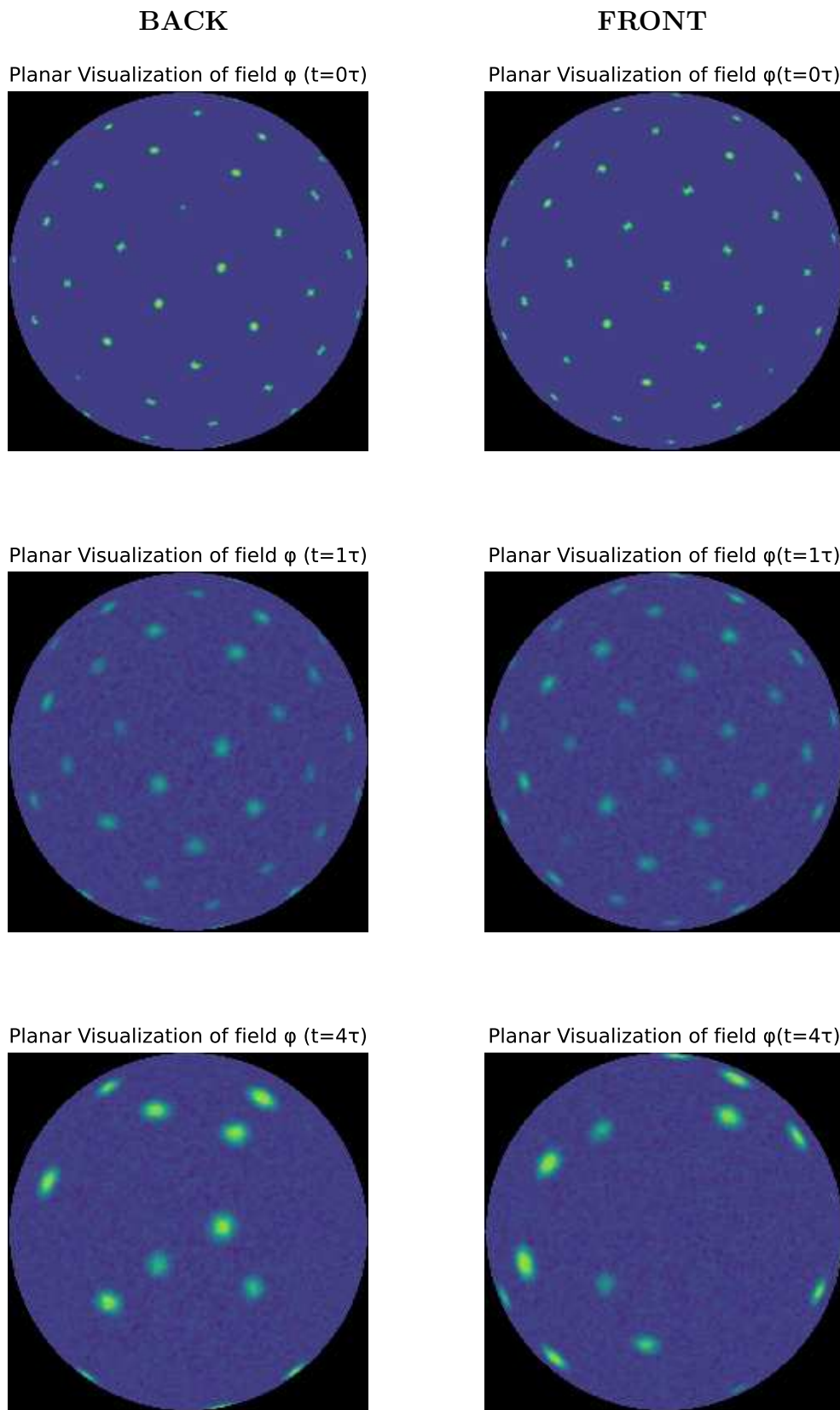


**Figure 6.13.** Heterogeneous nucleation and early coarsening stages. Planar visualization of field  $\varphi$  at the same time-steps of Fig. 6.10. The yellow spots represent high values of the field, so A is abundant in the regions in which the new domains are already formed ( $t=0\tau$ ) or survived ( $t=1\tau$  and  $t=4\tau$ ), while blue “sea” represents low values of the field (phase B). Field  $\varphi$  is visualized according to colorbar in Fig. 6.16.

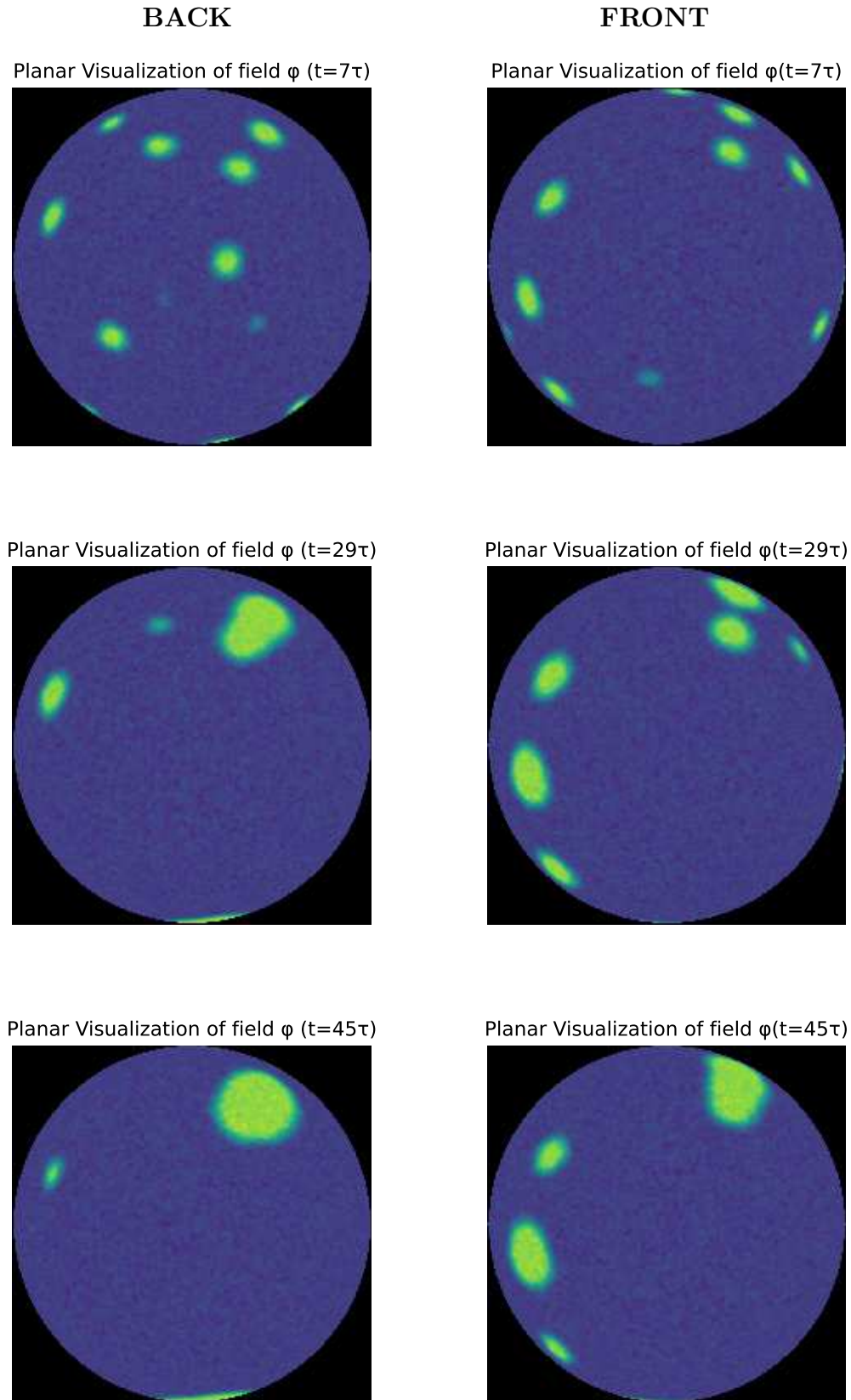


**Figure 6.14.** Coarsening stage. Planar visualization of field  $\varphi$  at the same time-steps of Fig. 6.11. The yellow spots represent high values of the field, so A is abundant in the domains that survive and grow, while it assumes lower values as time proceeds in the complementary regions. Field  $\varphi$  is visualized according to colorbar in Fig. 6.16.

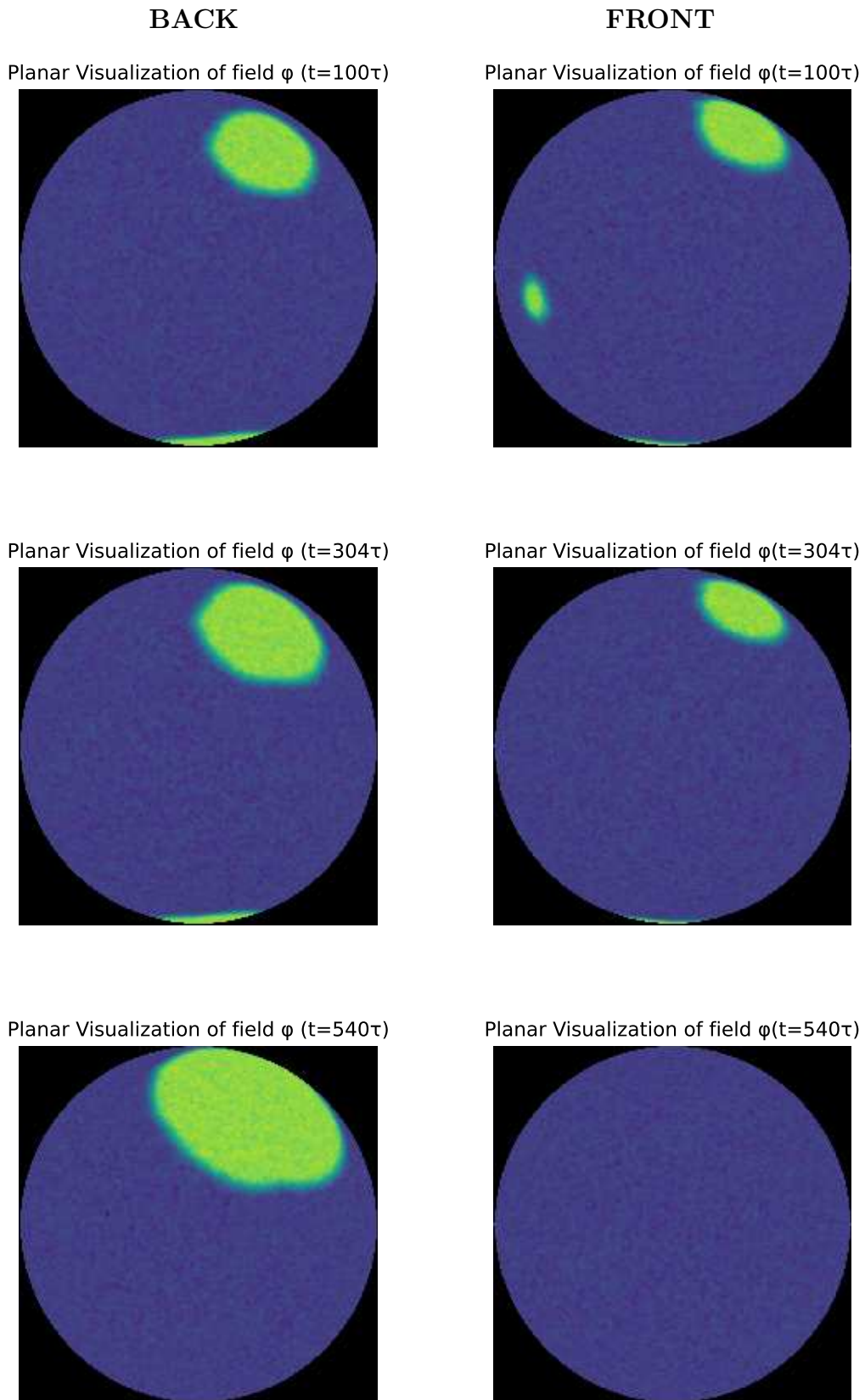


**Figure 6.15.** Late coarsening stage and relaxation to single-domain steady state. Planar visualization of field  $\varphi$  at the same time-steps of Fig. 6.12. The yellow spots represent high values of the field, so B is abundant in the regions of the vanishing domains (front), while A is abundant in the circular survived domain (back). Field  $\varphi$  is visualized according to colorbar in Fig. 6.16.

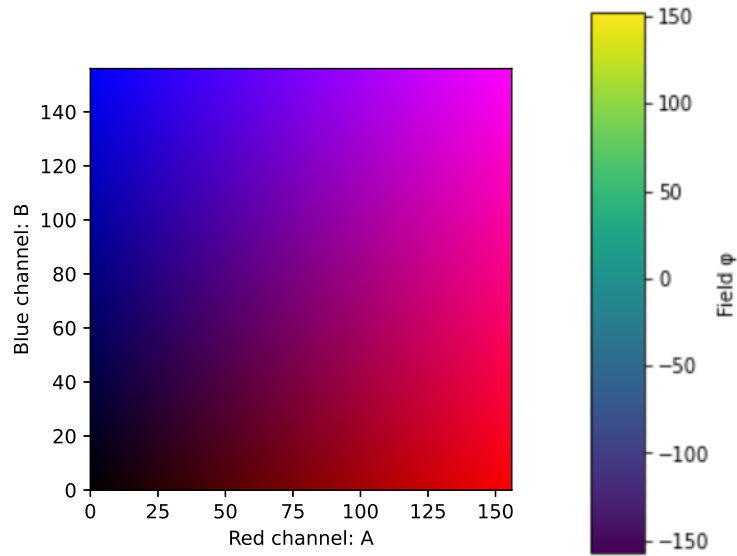


**Figure 6.16.** Color-map and color-bar. They show the relation between colors and number of molecules per site, in Fig. 6.10, 6.11, 6.12(color-map) and Fig. 6.13, 6.14, 6.15 (color-bar).

The same phenomenology of the homogeneous nucleation simulation, is observed. After the induced nucleation, the domains compete for the growth, at the beginning the coarsening is rapid, however, it slows down as competition gets stronger. Only one domain survives, whose shape is circular; a radial visualization of the field showing circularity of the last survived phase A domain is shown in Fig. 6.17.

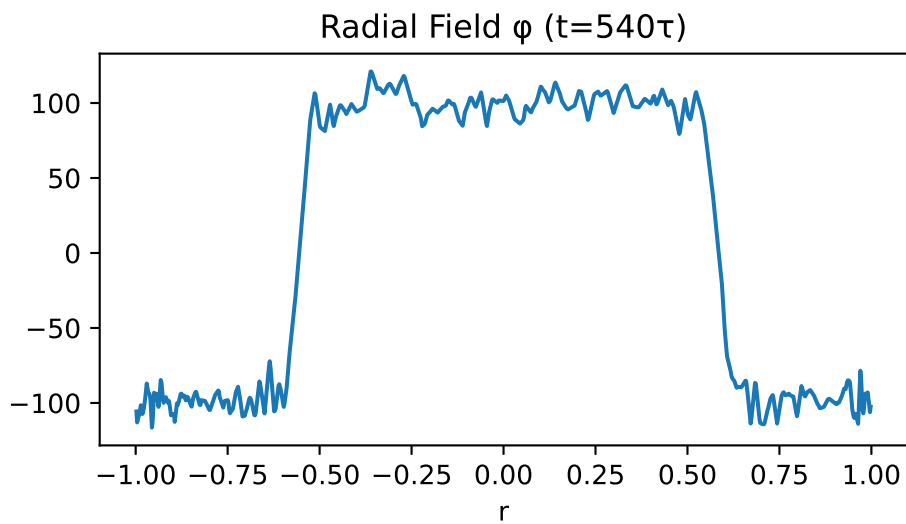


**Figure 6.17.** Radial visualization of field  $\phi$  at equilibrium ( $t = 540\tau$ ), showing that the phases occupy two distinct regions of the surface.

### 6.2.2 Domain coalescence

We have seen that the number of domains reduces due to coarsening. However this is not the only mechanism by which the number of domains reduces, in fact two or even more domains can fuse together to generate a larger and more stable one. This fusion event is called *coalescence*, and it's a phenomenological evidence of the existence of a *interfacial tension*, since it is responsible for perimeter length reduction of the interface between two phases.

In this section we are going to show that our model reproduce such coalescence events, in both homogeneous (Fig. 6.18, 6.19) and heterogeneous nucleation (Fig. 6.20, 6.21) case.

Visualizing field and single phase dynamics, we notice fusion events occur, similar to that one in Fig. 4.2. Two domains of phase A fuse together, assuming a shape resembling that one of the original smaller domains, however as time proceeds the it assumes a more circular shape (Fig. 6.18, 6.19, 6.20, 6.21).

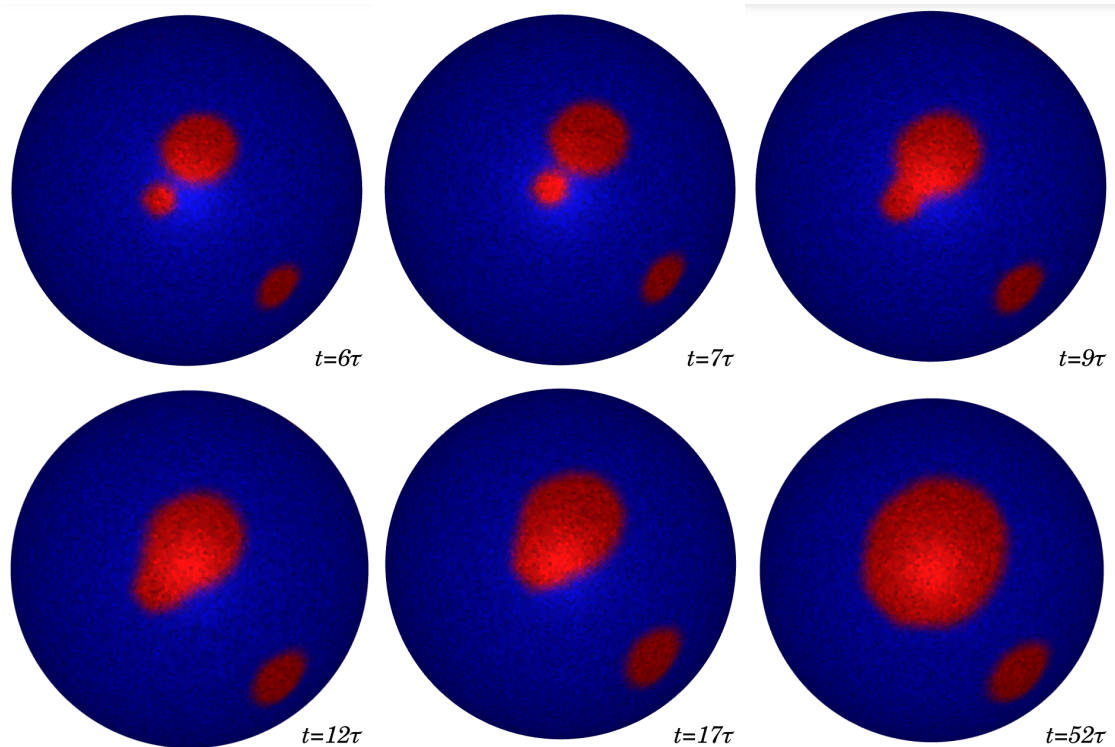


**Figure 6.18.** Coalescence of two phase A domains (homogeneous nucleation case). Two phase A domains (red), initially separated at  $t = 6\tau$ , fuse together as time goes on. The shape of new formed domain initially resembles that one of the separated domains ( $t = 7\tau, 9\tau, 12\tau, 17\tau$ ), but at  $t = 52\tau$  it assumes a circular shape. The single phases are visualized in two different color channels (red for A, blue for B) at each time-step  $\tau$ , according to colormap in Fig. 6.8.

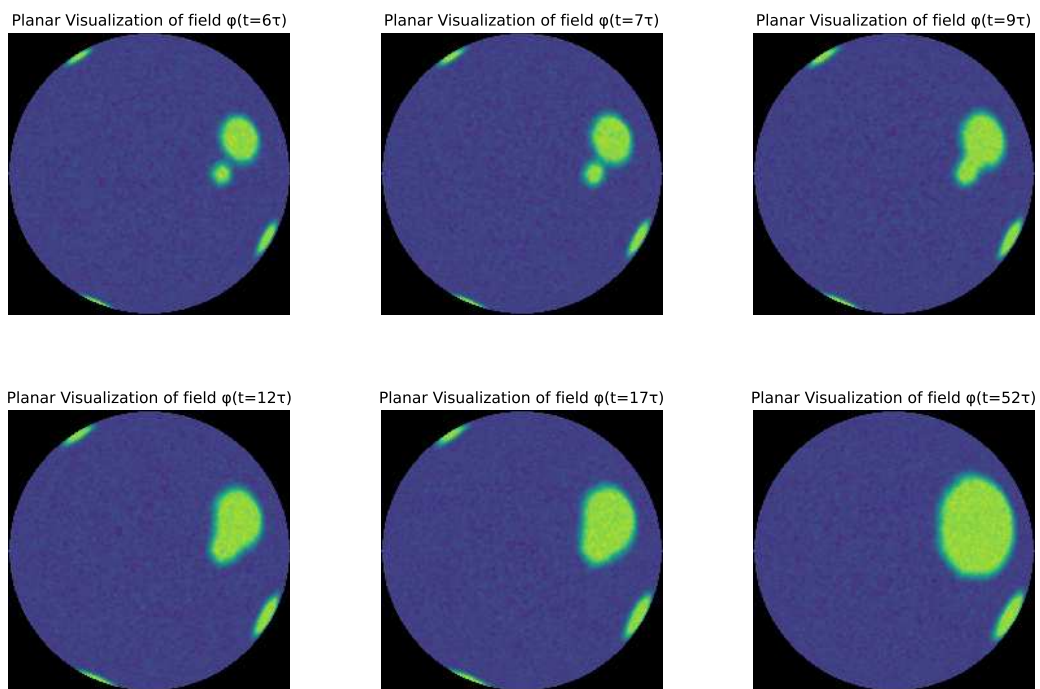


**Figure 6.19.** Coalescence of two phase A domains (homogeneous nucleation case). Planar visualization of field  $\varphi$  during coalescence of two phase A domains, at the same time-steps of Fig. 6.18. The yellow spots represent high values of the field, so A is abundant in the two initially separated domains ( $t = 6\tau$ ). As time proceeds they fuse together in a larger domain whose shape become circular ( $t = 7\tau, 9\tau, 12\tau, 17\tau, 52\tau$ ). Notice that the two fusing domains are the same of Fig. 6.18, they are simply visualized from an other point of view. Field  $\varphi$  is visualized according to colorbar in Fig. 6.8.

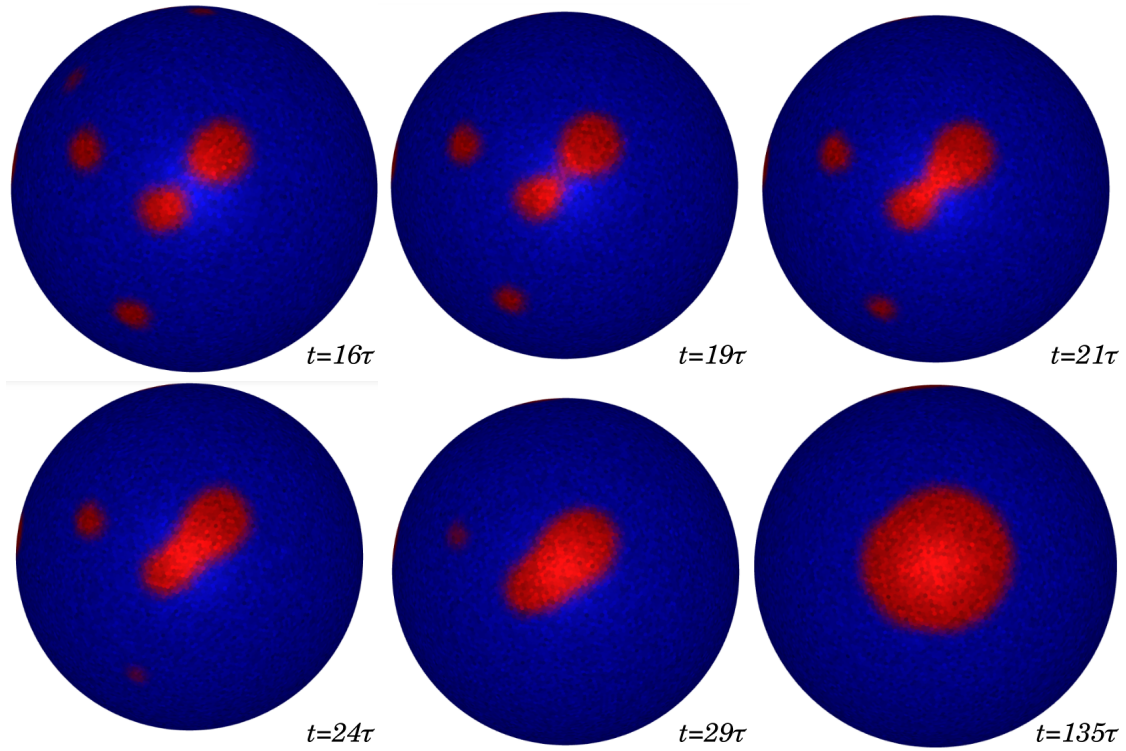


**Figure 6.20.** Coalescence of two phase A domains (heterogeneous nucleation case). Two phase A domains (red), initially separated at  $t = 16\tau$ , fuse together as time goes on. The shape of new formed domain initially resembles that one of the separated domains ( $t = 19\tau, 21\tau, 24\tau, 29\tau$ ), but at  $t = 135\tau$  it assumes a circular shape. The single phases are visualized in two different color channels (red for A, blue for B) at each time-step  $\tau$ , according to colormap in Fig. 6.16.

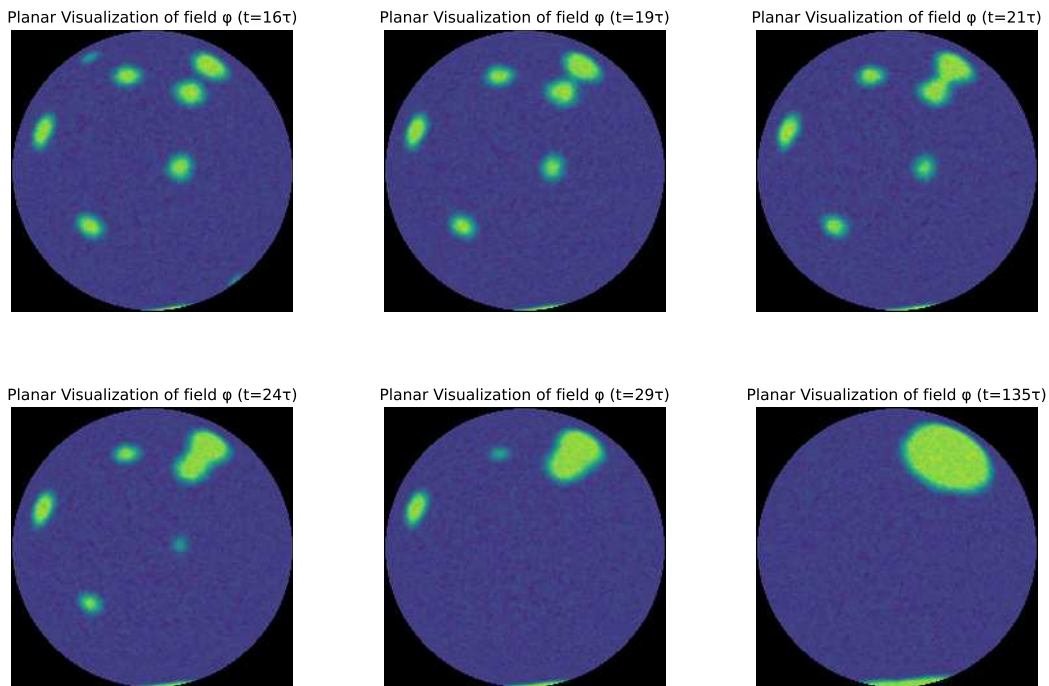


**Figure 6.21.** Coalescence of two phase A domains (heterogeneous nucleation case). Planar visualization of field  $\varphi$  during coalescence of two phase A domains, at the same time-steps of Fig. 6.20. The yellow spots represent high values of the field, so A is abundant in the two initially separated domains ( $t = 16\tau$ ). As time proceeds they fuse together in a larger domain assuming a circular shape ( $t = 19\tau, 21\tau, 24\tau, 29\tau, 135\tau$ ). Notice that the two fusing domains are the same of Fig. 6.20, they are simply visualized from an other point of view. Field  $\varphi$  is visualized according to colorbar in Fig. 6.16.

The presence of such coalescence events, the similarities between the phenomenology of our model and the classical one, and the similar profile representation of the order parameter, strongly suggest that our model could be considered a valid alternative to explain phase separation on membranes. However, to further confirm this suggestion, quantitative evaluation of the interfacial tension, and parameters dependency of fundamental quantities will be provided in the following discussion.

### 6.3 Single domain growth

In order to study our model in a more quantitative way, we are going to study the time evolution of a single domain size (visualization of field dynamics in Fig. 6.22). In order to do this, we perform simulations using the parameters of case 3 in Table 6.1. In particular, from such simulations, we will be able to compute the domain radius at different times and compare its behavior with the theoretical one (Fig. 6.23).

From numerical estimation of  $\gamma$ , we will also be able to find a numerical value for the interfacial tension. We will also infer the dependence of interface width on diffusivity. Finally, we will verify that the number of domains decreases over time with the theoretical power law dependence [6].

All the quantities that will be computed are expressed in microscopic unit used by the simulation program.

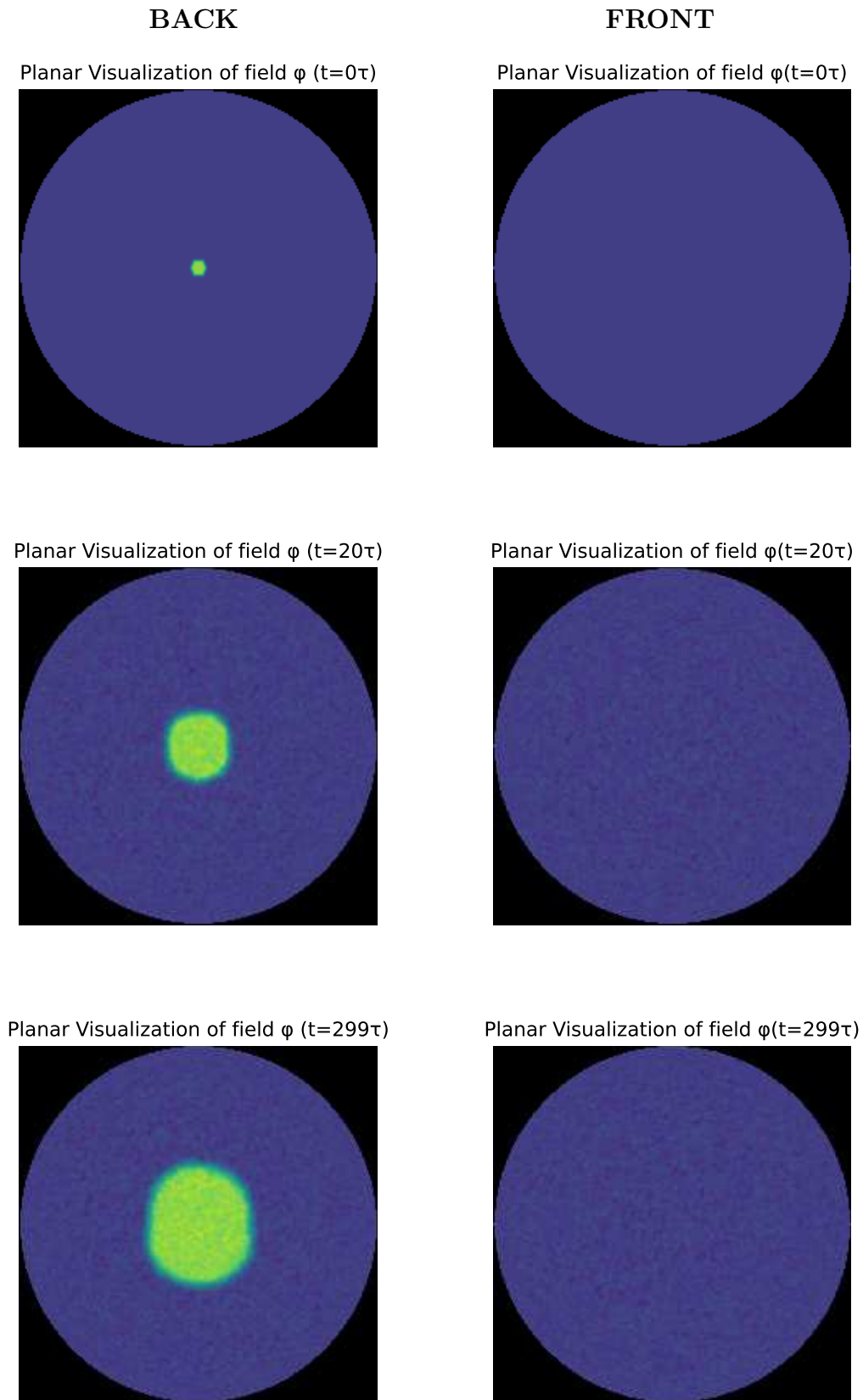


**Figure 6.22.** Single domain growth. Planar visualization of field  $\varphi$ , has been performed at  $t=0\tau, 20\tau, 299\tau$ . At  $t=0\tau$  the initial condition prescribing the initial domain of size  $R_i = 1.62$ , is shown. As time proceeds, being the initial domain size above the critical size ( $R_c^* \sim 1$ ), it grows and reach a size of  $R \sim 8.3$  at  $t=20\tau$ , and  $R \sim 14$  at  $t=299\tau$  (steady state). Field  $\varphi$  is visualized according to colorbar in Fig. 6.16.

### 6.3.1 Comparison between numerical and theoretical domain growth dynamics

In order to compute the radii at different times, we studied the time evolution of a single domain composed by only the A phase. From the system configurations at different times  $t$ , the areas and the corresponding radii are computed as written below:

$$S_w(t) = \frac{\sum_i A_i(t) a_i}{A_{\max}} \simeq \frac{a}{A_{\max}} \sum_i A_i(t)$$

$$\Rightarrow R = \sqrt{\frac{S_w(t)}{\pi}} \quad (6.2)$$

Where  $S_w(t)$  is the weighted area of the domain at time  $t$  (computed restoring the natural unit of length and time used by the program (Sec. 6.1.1)),  $A_i$  is the number of the total number of free and bound membrane-bound in face  $i$ ,  $a_i$  is the area of each face, that for simplicity is assumed to be equal for all the faces composing the spherical surface (6.1). The areas are weighted taking into account the maximum number  $A_{\max}$  of free and bound A per site among all the system configurations. In (6.2), we assumed that the domains are small and circular, so the curvature of the surface can be neglected and considered as planar.

The radii can now be computed. The same simulation has been repeated 5 times, and mean values of the radii with their standard deviation are computed and plotted (black dots in Fig. 6.23).

In order to compare the theoretical behavior of radii dynamics with the one emerging from the simulations, we fitted numerical values of the radii from  $t \sim 37$  to  $t \sim 282$  (Fig. 6.23) with Eq. 5.32, treating diffusivity as an unknown parameter. The fitting procedure provides a good agreement between the theoretical curve and data points for a value of diffusivity comparable to that one used in the simulations ( $D \sim 0.225 \pm 0.001$ ). Fitted curve is shown in Fig. 6.23.

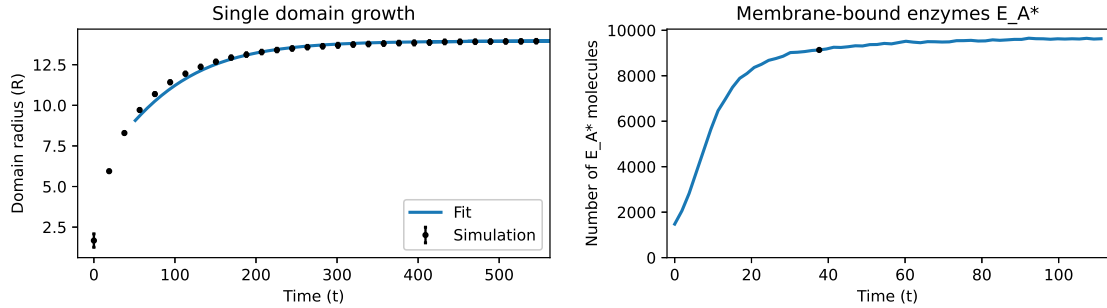


**Figure 6.23.** Fit of the predicted asymptotic behavior (5.32) with simulated single domain growth. (Left) The blue curve represents the predicted asymptotic behavior (5.32), while the black dots represent numerical data. The fit has been performed starting from the time when the number of bound enzymes reaches 95% of its asymptotic values. (Right) Number of enzymes  $E_A^*$  is plotted as function of time  $t$ . At  $t \sim 37$  the amount of enzymes is 95% of its equilibrium values.

We remark that, to perform the fit, we can't consider the initial values for the radii, since the concentration of bound enzyme ( $E_A^*$ ) is far from equilibrium. We therefore considered as initial value for the fit, the radius for which the enzymes have reached the 95% of their equilibrium value.

For large times, the concentration of enzymes bound to the A phase tends to a constant value, 5.21 holds.

On the other hand, since the curve that we want to fit has a singularity for  $R = R_{\text{eq}}$ , the values for the radii for the later times can create some numerical problem in the function used for the fit.

### 6.3.2 Measure of interfacial tension

In order to numerical estimate the interfacial tension, we first need a numerical estimation of  $\gamma$ .

Recalling that:

$$\gamma \simeq \frac{4\bar{B}^2}{3\delta} \quad (6.3)$$

Where  $\bar{B}$  (easily estimated) is the mean value of concentration of phase B far from the domain of phase A, and  $\delta$  is obtained fitting Eq. 5.37 with the steady-state radial profile of field  $\varphi$  (Fig. 6.24). Mean values and standard deviations are computed performing  $n=3$  simulations with different random seeds.

*Interfacial tension* can now be estimated, recalling that  $\sigma = \frac{\gamma D}{2}$ , and using the value for the diffusivity of Table 6.1 in case 3, we find  $\sigma \sim 1034 \pm 69$ .

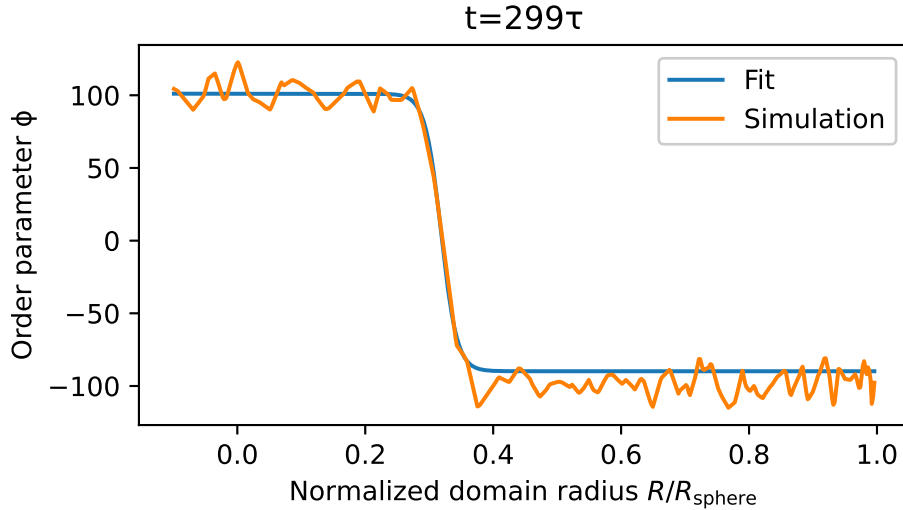


**Figure 6.24.** Radial field compared to the fitted one. Orange curve represents steady-state radial visualization of field  $\varphi$  (number of molecules per face). The blue line represents a curve obtained fitting the data points composing the orange line, with Eq. 5.37

### 6.3.3 Parameter dependence of interfacial tension

In the present section we are going to study the dependence of numerical values of width ( $\delta$ ) and tension ( $\sigma$ ) on diffusivity ( $D$ ). Then, we are going to compare such behavior with the theoretical one in (5.36). In particular, to investigate the dependence on diffusivity, we are going to perform simulations of a single growing domain with different values of diffusivity (the remaining parameters values are those in Table 6.1 for case 3), and extract the values of the interface width for each value of diffusivity.

From the fit of the radial field distribution ( $\varphi$ ) with Eq. 5.37, mean values and standard deviations of  $\delta$  are obtained for different values of diffusivity, taking into account  $n=3$  simulations with different random seeds. Such values are then fitted with  $\delta = hD^{\alpha_f}$ , where  $h$  and  $\alpha$  have to be found. The fitting procedure gives  $\alpha_f \sim 0.45 \pm 0.02$ , which is in good agreement with the expected one ( $\alpha_{th} = 0.5$ ).

Recalling that  $\sigma$  depends only on width and diffusivity:

$$\sigma = \frac{2\bar{B}^2}{3\delta}D$$

We find that also  $\sigma$  depends on diffusivity with an exponent which agree with theoretical expectations ( $\beta_f \sim 0.55 \pm 0.02$  vs  $\beta_{th} = 0.5$ ). Where  $\sigma \propto D^{\beta_f}$ .

The fitted curve for  $\delta$  and relative data points are shown in Fig. 6.25.

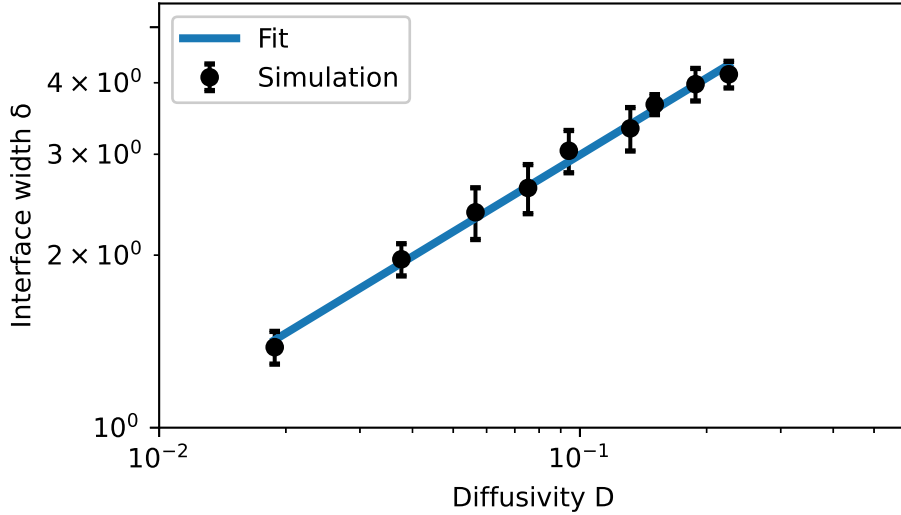


**Figure 6.25.** Interface width  $\delta$  versus diffusivity  $D$ , numerical points and fitted curve. Numerical values for  $\delta$  (black dots with error-bars) are fitted with a power law function of  $D$ , with exponent  $\alpha_f$ , whose value is  $\alpha_f \sim 0.45 \pm 0.02$ . Numerical values and fitted curve are plotted in log-log scale. Values for  $\delta$  and  $D$ , are expressed in microscopic units (Sec. 6.1.1).

We finally remark that for higher values of  $D$ , phase A domain doesn't form. This happens, because diffusion of molecules of A species toward sites occupied by phase B, gets stronger than autocatalytic feedback loop for phase A, that is not able to concentrate molecules of type A in a finite region of space.

## 6.4 Multiple domain growth

In this section we are going to compare the time evolution of the number of phase A domains, with the theoretical one [6].

We have already anticipated that the number of domains decreases over time, due to coarsening, but how it decreases over time hasn't been revealed yet. In Ref. [6], theoretical time evolution of the number of domains is derived in the context of Landau-Ginzburg approach. The number of domains decreases with a power law, function of time with exponent  $\gamma = -1$ , i.e. ( $N_d \propto t^{-1}$ ).

Simulations of multiple domains growth, with the same parameter values used for heterogeneous nucleation simulations (Table 6.1, case 2), have been performed. The number of domains have been counted at each time  $t$ , and its behavior over time has been fitted with  $N_d = \text{const} \cdot t^{\gamma_f}$ .

We found  $\gamma_f \sim -1.04 \pm 0.04$  which is in good agreement with theoretical predictions ( $\gamma = -1$ ). Numerical values of number of domains and fitted curve are shown in Fig. 6.26.





## Chapter 7

# Experimental investigation of Rab5-Rab11 co-localization in endosomes

Macromolecules (proteins, RNA...) can migrate between cellular compartments by vesicular transport. Biological material (cargo) is engulfed into endosomes, distinct membrane-bound endocytic organelles, which acting as shuttles permit material exchange between compartments, maintaining intracellular homeostasis [16]. There are three different types of endosomes: early endosomes (EE), recycling endosomes (RE) and late endosomes (LE). EEs, primarily marked by Rab5 proteins, are responsible for the initial engulfment of the cargo. REs, primarily marked by Rab11 proteins, are responsible for cargo migration to the plasma membrane. LEs, primarily marked by Rab7, are responsible for cargo transportation to the lysosomes and degradation [8]. Early endosome can mature into recycling and late endosomes, such maturation stages are characterized by changes in Rab proteins concentrations, depending on the kind of maturation. Therefore during maturation, such signaling proteins (Rab5, Rab11, Rab7) can be present in different amounts on the same endosome membrane and eventually form domains [13].

To detect domains formation of such proteins on endosome membranes, co-localization of signaling proteins on the same endosome membrane need to be studied. In Ref. [13], co-localization study of fluorescent signals of Rab5, Rab4, Rab11 proteins on the same endosome has been performed.

During my internship at “IRCCS” Candiolo, I focused on a preliminary investigation, trying to set up a robust protocol for immunofluorescence (IF), that could be used to visualize Rab proteins located into glioblastoma cancer cells (U251-MG). The protocol should allow a clear visualization of the proteins, featuring a low background (aspecific) fluorescent signal (further details in Sec. 7.1). Once the protocol has been set (Appendix A), I used it to study co-localization of Rab5 and Rab11 proteins on glioblastoma cancer cell model (U251-MG), in different conditions, in order to study Rab5-Rab11 axis (interaction).

## 7.1 Immunofluorescence technique

Immunofluorescence is a technique that permits visualization of various cellular antigens (like proteins), using fluorophores-conjugated antibodies that have high affinity to the targets of interest. In our experiments, we adopted the “indirect staining”: we used antibodies linking to Rab5 and Rab11 (primary antibodies: 1Ab), and then we used fluorophores-conjugated secondary antibodies (2Ab) linking to the primary ones, to visualize fluorescent signals. So the fluorescent signals detected with a light microscope show the presence of the secondary antibodies, that with a certain affinity have been bound with their targets. Such indirect staining may lead to a detection of aspecific background signals, due to high concentration of 2Ab, or low affinity between 2Ab and 1Ab.

Since Rab proteins are located inside the cell, permeabilization of the membrane is needed in order to let the antibodies penetrate inside the cell and link to their targets. A non optimal permeabilization, could lead to a huge detection of aspecific signals, since the antibodies have not penetrated optimally and didn't bind to their targets.

In our case the IF protocol is said to be well set when clear fluorescent signals of Rab proteins can be detected with the lowest aspecific signal detection. This is done, testing various secondary antibodies dilutions, and different membrane permeabilization techniques.

The optimized protocol is shown in Appendix A. In Fig. 7.1, visualization of a single cell stained for Rab5 and Rab11 proteins, is provided.

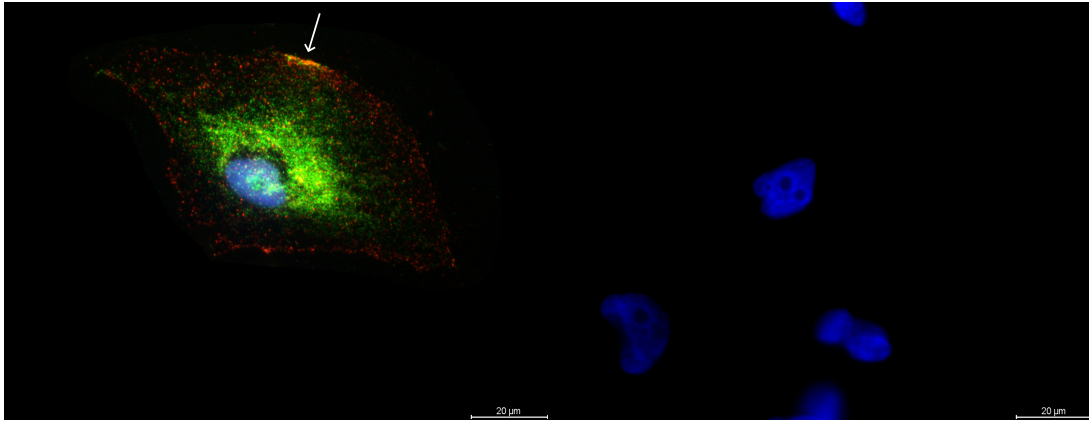


**Figure 7.1.** (Righth) Rab5-Rab11 (yellow) co-localization detection. Using IF protocol in Appendix A, cells are stained for Rab5 (red), Rab11 (green) proteins, and DNA (nucleus in blue). IF protocol allows to minimize background signals (red and green) at least in the peripheral regions of the cells. We can appreciate a good co-localization signals on the upper peripheral region (white arrow). (Left) Negative control for IF experiment. No green or red fluorescent signal is detected. Fluorescence signals detection is performed with LEICA light microscope, and images are taken with 100X objective, to visualize single cells.

## 7.2 Colocalization study

Recalling that Rab5 protein is a marker for early endosomes, while Rab11 marks recycling endosomes, a co-localization between Rab5 and Rab11 denotes the maturation process from early to recycling endosomes, i.e the recycling of the transported cargo.

We used the IF protocol to study Rab5 and Rab11 fluorescent signals co-localization in 15 (U251-MG) cells, in two different conditions. In the first one, IF was performed on cells in their physiological conditions, in the second one IF was performed on cells that were treated with cetuximab ( $10\mu\text{g}/\text{mL}$  over night). Cetuximab is an anti EGFR antibody used in pharmacological treatment of cancers, that inhibits the action of EGF (epidermal growth factor), linking to its receptor (EGFR) and carrying it to the lysosome. Cetuximab plays an important role on the fate of EGFR that can be seen as a cargo for the endosomes. It is expected that cells treated with cetuximab show lower Rab5 and Rab11 co-localization, since EGFR has been degraded. In order to verify such hypothesis co-localization study was performed in two different ways:

- Rab5 and Rab11 co-localization over the entire cell surface (Total co-localization)
- Rab11 co-localization only on positive Rab5 signal (Co-localization over Rab5 ROIs)

Where the ROIs (regions of interest) are the portions of the images in which high fluorescent signals of Rab protein are detected.

Such co-localization studies are performed extracting a Pearson correlation coefficient (PCC) based on pixel proximity of the two signals (red for Rab5, green for Rab11). PCCs are obtained using imaging software (ImageJ, ICY and LASx visualizer). In particular ICY contains a tool for co-localization study that compute PCCs between signals over selected portions of the cell image.

Rab proteins co-localization is stronger in the perinuclear regions, since in that region a lot of proteins are stored in Golgi apparatus and endoplasmic reticulum. Nevertheless, we are interested in endosomes, which are located in the peripheral part of the cells. Therefore, ICY tool for co-localization study is used ignoring the nuclear and perinuclear portions of cell.

Mean values of PCCs and relative standard deviations are summarized in Fig. 7.2.

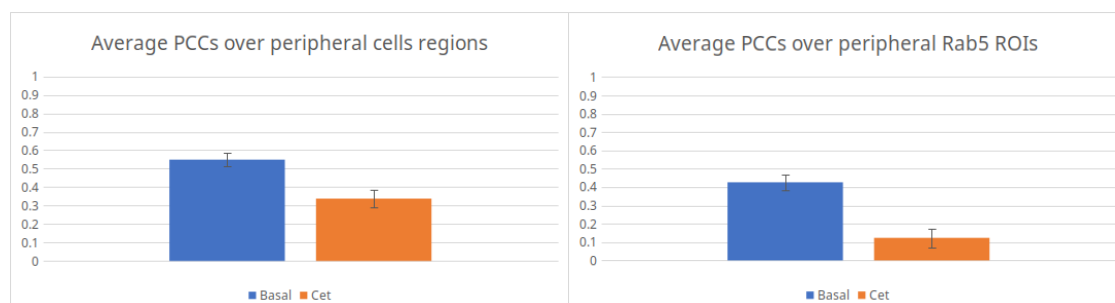


**Figure 7.2.** Estimation of Rab5-Rab11 co-localization in standard conditions (Basal) and cetuximab treatments (Cet), over peripheral regions and peripheral Rab5 ROIs. Mean values and standard deviations of Pearson correlation coefficient (PCC), quantifying red and green pixel-based signals co-localization, have been computed with ICY software.

### 7.3 Interpretation of the experimental results

Analysis reveals what was expected: cetuximab treatment lowers co-localization between Rab5 and Rab11. Cetuximab is an antibody linking to EGFR carrying it to the lysosome, where it is degraded. In standard conditions, EGFR is recycled, therefore Rab5-Rab11 recycling axis works, infact we see co-localization between RAB5 and RAB11. On the other hand, in cells treated with cetuximab, EGFR has been mostly carried to the lysosomes and degraded, therefore Rab5-Rab11 recycling axis has been suppressed, and co-localization between Rab5-Rab11 is has diminished.

### 7.4 Limitations of the study

My experimental investigation is preliminary: we are not sure that detected co-localization of the two Rab proteins occurs on the same endosome because we don't have information on endosome presence. Nevertheless, co-localization study over Rab5 ROIs far from the nucleus, constitutes a rough attempt to endosome marking because peripheral Rab5 mostly concentrates on endosomes. For this reason, our co-localization measurements are overestimated, in the sense that, among the selected Rab5 ROIs, some of them surely mark endosomes, but others not.

In order to be sure that co-localization occurs on the same endosome, we should mark also the cargo (EGFR) and study a triple co-localization on EGFR ROIs, marking the endosomes location, similarly to what has been done in [13].

We remark that such IF experiments provides information on the coexistence of Rab proteins on the same endosome, it can't be used to asses domains formation, since endosome size is comparable with the limit of resolution for light microscopy technique. Further information about Rab proteins domains formation can be obtained using electron microscopy techniques [13].



# Chapter 8

## Discussion

Phenomenology emerging from our model, is completely similar to that one prescribed by the classical phase separation. No matter what kind of nucleation has occurred, we will observe the same phenomenology: coarsening and relaxation to a steady-state single domain. The early coarsening is rapid, while the late coarsening is slow: the new born domains rapidly evaporate favoring the growth of the larger ones, however as time passes, the few survived domains becomes large, therefore it takes more time for the unfavoured domains to completely vanish.

Also fusion events (coalescence) between domains are observed: for the system is more favourable a situation in which the perimeter length of the interface between two phases is minimal (i.e circular). Coalescence is a phenomenological evidence of the existence of an interface tension: in classical phase separation, interface tension was responsible of interface energy decrease, leading to a minimization of the interface size between two phases. Therefore, observation of an interface size minimization in our model, leads us to believe that an interfacial tension exists.

At the end of the process only one circular domain survives, whose size does not increase anymore. The phase composing the last domain is in equilibrium with the other phase occupying the complementary region.

If one observe such phenomenology neglecting for a moment that we are describing a gas, he would say that he is observing phase separation in a liquid.

Such similarities suggested a phase field approach to the model. Within this framework parameters similar to those characterizing classical phase separation, emerged. We were able to find equations describing critical size and metastability degree which increasing and decreasing over time, as prescribed by the classical model. Moreover, we were able to find numerical estimation of the interface width and tension, and infer their dependency on diffusivity, ending up with a good agreement between theoretical predictions and simulations.

Finally we focused on the time evolution of the number of domains, and we discovered that it decreases over time as a power law with an exponent compatible to that one predicted by theory.

Phase separation paradigm can explain domains formation on endosome membranes of Rab proteins. Preliminary experimental investigation about such domains formation has been performed. An Immunofluorescence protocol, used to visualize Rab5-Rab11 co.localization on peripheral regions of glioblastoma cancer cells, has been set in different cell conditions. Such co.localization study revealed the expected results. Nevertheless, our experimental investigation cannot explain domains formations of such Rab proteins on the same endosome membrane, but it constitutes a good starting point for further investigation.



# Appendix A

## Experimental Materials and Methods

### Materials:

- Phosphate Buffered Saline (PBS) 1x
- Saponin solution: Saponin 0.05% (w/v) in PBS
- 24-Multiwell
- Paraformaldehyde(PFA) 4%
- U251-MG cells
- 2 circular slides
- Microscope slide
- Solution 1: NH<sub>4</sub>Cl 50 mM in PBS
- Needle and tweezers
- Solution 2: BSA (Bovin serum albumin) 1%(w/v) in PBS
- Primary Ab: Rab5 (mouse). <https://www.bdbiosciences.com/en-us/products/reagents/microscopy-imaging-reagents/immunofluorescence-reagents/purified-mouse-anti-rab5.610725>
- Primary Ab: Rab11 (rabbit). <https://www.cellsignal.com/products/primary-antibodies/rab11-d4f5-xp-rabbit-mab/5589>
- Solution 1:100 of Rab5 and/or 1:100 Rab11 in BSA 1% (double/single staining). (See aliquots)
- Secondary Ab: Anti-mouse (Red) <https://www.sigmaaldrich.com/IT/it/specification-sheet/SIGMA/43394>
- Secondary Ab: Anti-rabbit(Green) <https://www.sigmaaldrich.com/IT/it/product/sigma/18772>
- Solution 1:3000 of Secondary Ab mouse in BSA 1% and/or 1:200 of Secondary Ab rabbit (double/single staining).(See aliquots)
- DAPI: <https://www.sigmaaldrich.com/IT/it/product/roche/10236276001>
- Solution 3: DAPI 1 $\mu$ g/mL in solution 2.
- Mounting medium: <https://www.thermofisher.com/order/catalog/product/00-4958-02>

**Aliquots:**

- Aliquot 1: Aliquot in solution 2 the primary Abs (Rab5 e/o Rab11), at the suggested concentration. ( $70\mu L$  for one treated slide)
- Aliquot 2: Aliquot in solution 2 the secondary Abs (a-mouse and/or a-rabbit), at the suggested concentration. ( $140\mu L$  for one treated slide)

**Execution (Single/double staining):**

- Place two circular slides in 24-multiwell, 1 will be the negative control, the other the treated.
- Plate 50.000 cells in each slide (cells in DMEM-FBS solution). (Number tested for U251-MG)
- Incubate over night (O.N)
- Remove DMEM-FBS and wash with PBS solution,  $500\mu L$  for each well.
- Remove PBS and wash again in PBS
- Add saponin solution for 4 min at  $4^{\circ}C$ ,  $500\mu L$  for each well.
- Remove saponin, and add PBS
- Remove PBS and wash in PBS at  $4^{\circ}C$  (repeat other 2 times)
- Fix with PFA 4% for 20 min at  $4^{\circ}C$ ,  $500\mu L$  for each well.
- Remove PFA, and add PBS at  $4^{\circ}C$
- Remove PBS and wash with PBS at  $4^{\circ}C$ ,  $500\mu L$  for each well. (repeat other 2 times).
- Remove the slide from the wells using needle and tweezers, place them in a box, in absence of light.
- Quench with  $NH_4Cl$  solution for 20 minutes ( $70\mu L$  for each slide, covering the entire slide surface)
- Remove and wash with PBS ( $70\mu L$  for each slide) (repeat one more time)
- Incubate with solution 2 for 1h at  $25^{\circ}C$  ( $70\mu L$  for each slide).
- Remove solution 2 from the slide considered as treated one.
- Incubate treated slide with aliquot 1 for 1h30min at  $25^{\circ}C$ .
- Remove previous solution and wash with PBS (repeat 3 times)
- Remove solution 2 from the slide considered as negative control.
- Incubate both slides with aliquot 2
- Remove aliquot 2 and wash with PBS (repeat 4 times)
- Incubate with solution 3 for 5 min at  $25^{\circ}C$
- Remove previous solution and wash with PBS (repeat 2 times))
- Pour two droplets of mounting medium ( $\sim 2\mu L$  per droplet) on a microscope slide.
- Remove PBS from the circular slides.
- Place the slides on the droplets of mounting medium.
- Carefully apply a light pressure on the slides, using the needle (or tweezers), in order to uniformly distribute the mounting medium.

# Bibliography

- [1] Salman F Banani, Hyun O Lee, Anthony A Hyman, and Michael K Rosen. Biomolecular condensates: organizers of cellular biochemistry. *Nature Reviews Molecular Cell Biology*, 18(5):285–298, May 2017.
- [2] Clifford P Brangwynne, Christian R Eckmann, David S Courson, Agata Rybarska, Carsten Hoege, Jöbin Gharakhani, Frank Jülicher, and Anthony A Hyman. Germline P granules are liquid droplets that localize by controlled dissolution/condensation. *Science*, 324(5935):1729–1732, May 2009.
- [3] A. J. Bray. Theory of phase-ordering kinetics. *Advances in Physics*, 51(2):481–587, 2002.
- [4] Elisa Floris, Andrea Piras, Luca Dall’Asta, Andrea Gamba, Emilio Hirsch, and Carlo C. Campa. Physics of compartmentalization: How phase separation and signaling shape membrane and organelle identity. *Computational and Structural Biotechnology Journal*, 19:3225–3233, 2021.
- [5] Erwin Frey and Fridtjof Brauns. Self-organisation of protein patterns, 2020.
- [6] A Gamba, I Kolokolov, V Lebedev, and G Ortenzi. Universal features of cell polarization processes. *Journal of Statistical Mechanics: Theory and Experiment*, 2009(02):P02019, feb 2009.
- [7] Andrea Gamba, Antonio de Candia, Stefano Di Talia, Antonio Coniglio, Federico Bussolino, and Guido Serini. Diffusion-limited phase separation in eukaryotic chemotaxis. *Proceedings of the National Academy of Sciences*, 102(47):16927–16932, 2005.
- [8] Alex H Hutagalung and Peter J Novick. Role of rab GTPases in membrane traffic and cell physiology. *Physiol Rev*, 91(1):119–149, January 2011.
- [9] Kazuki Kohata and Daisuke Miyoshi. RNA phase separation-mediated direction of molecular trafficking under conditions of molecular crowding. *Biophys Rev*, 12(3):669–676, May 2020.
- [10] Andrea Musacchio. On the role of phase separation in the biogenesis of membraneless compartments. *The EMBO Journal*, 41(5):e109952, 2022.
- [11] Jochen Rink, Eric Ghigo, Yannis Kalaidzidis, and Marino Zerial. Rab conversion as a mechanism of progression from early to late endosomes. *Cell*, 122(5):735–749, September 2005.
- [12] Matteo Semplice, Andrea Veglio, Giovanni Naldi, Guido Serini, and Andrea Gamba. A bistable model of cell polarity. *PLOS ONE*, 7(2):1–14, 02 2012.
- [13] B Sönnichsen, S De Renzis, E Nielsen, J Rietdorf, and M Zerial. Distinct membrane domains on endosomes in the recycling pathway visualized by multicolor imaging of rab4, rab5, and rab11. *J Cell Biol*, 149(4):901–914, May 2000.
- [14] Xiaolei Su, Jonathon A Ditlev, Enfu Hui, Wenmin Xing, Sudeep Banjade, Julia Okrut, David S King, Jack Taunton, Michael K Rosen, and Ronald D Vale. Phase separation of signaling molecules promotes T cell receptor signal transduction. *Science*, 352(6285):595–599, April 2016.
- [15] A Veglio, A Gamba, M Nicodemi, F Bussolino, and G Serini. Symmetry breaking mechanism for epithelial cell polarization. *Phys Rev E Stat Nonlin Soft Matter Phys*, 80(3 Pt 1):031919, September 2009.
- [16] Ruud H Wijdeven, Marlieke L M Jongasma, Jacques Neefjes, and Ilana Berlin. ER contact sites direct late endosome transport. *Bioessays*, 37(12):1298–1302, October 2015.
- [17] David Zwicker, Anthony A. Hyman, and Frank Jülicher. Suppression of ostwald ripening in active emulsions. *Phys. Rev. E*, 92:012317, Jul 2015.